

# Why we see something rather than nothing

Tommy Anderberg\*

(Dated: May 12, 2012)

The low energy limit of standard electroweak theory is a partially gauged non-linear sigma model featuring rich non-perturbative dynamics. Numerical evidence for plasma oscillations, charge separation and long-lived extended configurations is presented, along with physical, analytic and numerical arguments for the existence of an attractor associated with the electrically neutral Goldstone boson. Its effect is to drive the effective photon mass to small (but probably finite) values, reducing the opacity of space to a fraction of what it would be if the Higgs field were uniformly distributed on its vacuum manifold.

PACS numbers: 11.15.Ex, 11.27.+d, 12.15.-y, 95.36.+x, 98.80.-k, 98.80.Cq

## I. INTRODUCTION

Simple questions can lead to deep insights. In 1823, Olbers asked why the sky is dark at night; in an infinite, static universe, every line of sight would end on a star, and the sky would be solid white. So the universe can not be infinite and static. In the 1970s, cosmologists asked how patches on opposite sides of the sky can have the same temperature; according to the big bang model, they were never in causal contact, and should therefore not be in thermal equilibrium. So the big bang model must be amended to overcome the limits of causality. These days, that amendment is widely believed to be an early era of exponential expansion (inflation).

In 2004, Penrose asked why we can see distant objects in optical telescopes [1].

The background to this question has a shared heritage with the previous one: the big bang model has a finite particle horizon, i.e. there is always a maximum distance within which information could have been exchanged. The other ingredient is the Higgs mechanism. According to the standard (well informed) view of electroweak theory, as the energy density of the universe dropped below the electroweak scale, ( $\sim 100 \text{ GeV}$ )<sup>4</sup>, the 4-component Higgs field  $\Phi$  settled at a randomly picked point  $\langle\Phi\rangle$  on the 3-sphere which defines its vacuum manifold [2]-[5], giving mass to three linear combinations of the four electroweak gauge bosons and leaving one massless: the photon. As this random choice of vacuum expectation value (VEV) could not be communicated beyond the particle horizon, it could not be coordinated across space. Instead,  $\langle\Phi\rangle$  started out with gradients on superhorizon scales and subsequently relaxed as the horizon grew.

This poses a problem. Quasars on opposite sides of the sky are still outside each other's particle horizons. Photons from them which reach us now therefore originated in regions with uncorrelated  $\langle\Phi\rangle$ , and must be assumed to have crossed at least one  $\langle\Phi\rangle$  gradient along the way. What happens to photons which cross such a gradient?

Simple questions are often asked, and answered, more

than once. What we now refer to as Olbers' Paradox seems to have been first formulated by Thomas Digges in 1576 [6]. In 1610, Kepler suggested that the solution must be a spatially finite universe.

The question about the fate of particles crossing  $\langle\Phi\rangle$  gradients was first asked by Weinberg in 1974 [4]. It was quickly answered for light by A. Everett, who treated the problem as one of classical wave transmission and found that the result depended on the width of the  $\langle\Phi\rangle$  gradient relative to the light's wavelength: total reflection from sharp gradients, total transmission across wide ones, partial transmission in intermediate cases [7]. Absent some reason to expect sharp gradients, there would therefore seem to be no observable consequences. Presumably because of this conclusion, the question then seems to have been forgotten for three decades. Everett's terminology may have played a part in this too; he used the term "domain wall" (along with "domain boundary") which has since become synonymous with "topologically stable two-dimensional defect passing through  $\Phi = 0$ ". The standard electroweak model does not have domain wall solutions, nor can any sensible alternative to it, since their large energy density would make them cosmologically disastrous [8][9].

Three decades later, Penrose brought up the issue again as a cosmological argument against the Higgs mechanism, predictably eliciting hasty dismissals from particle physicists. While unfortunate, this was perhaps understandable. If your focus is particle interactions in accelerator experiments, you are used to treating  $\langle\Phi\rangle$  as a mere constant. There are right reasons for this, and there are wrong reasons.

The wrong reasons start with the misunderstanding that the "classical" electroweak Lagrangian reproduced in countless introductory QFT textbooks describes physics on macroscopic distance scales. If you believe that, you implicitly believe that there are arbitrarily small fractions of massive  $W^\pm$  and  $Z^0$  bosons propagating over macroscopic distances. The "classical" electroweak Lagrangian is a *bare* Lagrangian. Its proper place is inside a Feynman path integral, plugged into an exponentiated action. To study the theory on macroscopic scales, you must first derive a low energy effective theory by integrating out the massive degrees of free-

---

\*Electronic address: Tommy.Anderberg@simplicial.net

dom. In the low energy, long distance limit, only the massless fields remain, and the massive degrees of freedom only affect the result through the renormalization of the massless fields and their couplings [10][11][12].

There is one context where the bare Lagrangian is a good leading order approximation to macroscopic physics: a plasma hot enough to maintain large occupation numbers for all massive fields (in particle physics terms, by the continuous creation of new, short-lived massive particles in collision events) [13][14][15]. This justifies the use of bare Lagrangians in the early, hot universe. But in the old, cold universe where we live, we must use a low energy effective theory.

It is a short step from believing that a bare Lagrangian describes macroscopic physics to believing that you can conveniently set all but one component of the macroscopic quantity  $\langle\Phi\rangle$  to zero by imposing the unitary gauge. Introductory QFT textbooks often claim this explicitly, but fail to properly emphasize that this trick only works for small perturbations about a given, constant  $\langle\Phi\rangle$  (if at all). In the general case, it has been well understood at least since the 70s that the transformation to the unitary gauge is singular [16][17][18] (see p. 442 in [19] for an example of a textbook which does point this out). The reason is that the electroweak sector of the Standard Model has a rich non-perturbative structure [20]-[30] which clashes with the topological triviality imposed by the unitary gauge. It is therefore not correct to use the bare Lagrangian in the unitary gauge to derive an effective low energy theory (in practice, this fails due to the non-renormalizability of the resulting perturbative expansion) nor is it correct to quantize perturbations about “classical” configurations derived from it (because the bare Lagrangian is not a good first approximation to macroscopic physics, unless you happen to be doing high temperature field theory).

Non-perturbative work in gauge field theories with SSB is instead usually done in an axial gauge, which amounts to setting one component of each gauge field to zero.  $\Phi$  is involved only indirectly, through the equations of motion for the time-like components of the gauge fields, which become algebraic constraints (essentially Gauss’ law; see e.g. p. 15 in [19]). For numerical work, the time-axial (a.k.a. temporal) gauge is particularly convenient, and therefore ubiquitous [31]-[37]. It is also used in this paper.

The right reason to assume a constant  $\langle\Phi\rangle$  in particle physics has nothing to do with the unitary gauge and everything to do with energy density. Since the Lagrangian is quadratic in derivatives of  $\Phi$ , a smooth gradient in  $\langle\Phi\rangle$  extending over some length scale  $L$  can be expected to have an energy density  $\sim \nu^2/L^2$ , where  $\nu \simeq 246.3 \text{ GeV}$ . With  $L = 1 \text{ m}$ , this translates to roughly  $10^{10} \text{ J/m}^3$ , equivalent to the explosive yield of a couple tons of TNT per cubic meter. If isolated (and not stabilized by something else), such a gradient would relax to the surrounding  $\langle\Phi\rangle$  under emission of electromagnetic radiation and fermions on a timescale  $\propto L$  ( $10^{-9} \text{ s}$  for

$L = 1 \text{ m}$ ). Since the universe is believed to have been cooling for  $\sim 10^{10}$  years, and since we do not see space exploding in our immediate neighborhood, it is reasonable to expect  $\langle\Phi\rangle$  to be effectively constant on length scales  $L \ll 10^{10}$  light years, such as those of accelerator experiments.

In 2005, having read [1] and knowing the criticism to be incorrect, but (fortunately?) unaware of Everett’s work, I derived an expression for residual luminosity across a  $\langle\Phi\rangle$  gradient, essentially by projecting the photon (i.e. massless) state at the source onto the photon state at the observer’s location, to find

$$\ell(\vec{\omega}) = \sin^2(\theta_W) \frac{\omega_{\perp}^2 \cos(|\vec{\omega}|) + \omega_3^2}{|\vec{\omega}|^2} + \cos^2(\theta_W) \quad (1)$$

where  $\vec{\omega} = [\omega_1, \omega_2, \omega_3]$  are the SU(2) parameters relating  $\langle\Phi\rangle$  in the two domains,  $\omega_{\perp}^2 = \omega_1^2 + \omega_2^2$  and  $\theta_W$  is the Weinberg angle [38] (see Appendix A for the original derivation).

Unlike Everett’s, this is a quantum mechanical answer. The physical picture is of two large regions with constant but different  $\langle\Phi\rangle$ , separated by an interpolating boundary smooth enough to make reflection negligible. As it traverses the boundary, the photon becomes a linear combination of electroweak gauge bosons, and given enough energy (at least enough to put a neutrino pair on shell), the massive part of the mix decays to fermions. It is not necessary to consider the details of the decay, since it is clear that it will occur at some point in the destination region (and quickly, given the time scale of electroweak interactions,  $\sim 10^{-27} \text{ s}$ ).

Assuming that  $\langle\Phi\rangle$  is evenly distributed on its vacuum manifold, it is also easy to derive a probability distribution function (PDF) for  $\ell(\vec{\omega})$  (see Appendix B). The surprisingly simple result is a step function  $> 0$  for  $\ell \in [1 - 2 \sin^2(\theta_W), 1]$ , with average

$$\langle\ell\rangle = 1 - \sin^2(\theta_W) = \cos^2(\theta_W) \simeq 0.77 \quad (2)$$

This happens to almost exactly match the observed luminosity deficit of SNe Ia at redshift  $z \sim 0.5$ , the point of greatest leverage on the inferred value of the cosmological constant  $\Lambda$ . Rather than being an argument against the Higgs mechanism, cosmological  $\langle\Phi\rangle$  gradients therefore seemed to offer an economical explanation of supernova observations based on Standard Model physics only.

But they could easily be a problem too.  $\langle\Phi\rangle$  gradients carry conserved quantities (energy, momentum, electric charge) which must go elsewhere, i.e. to fermions, upon relaxation. Fermions can only be produced effectively while the energy and charges within the Compton volume of a fermion pair (e.g. electron + anti-neutrino) equal or exceed the total mass and charges of such a pair (on shell). Once  $\langle\Phi\rangle$  gradients fall below this threshold, dissipation to fermions becomes exponentially suppressed. Random charged  $\Phi$  configurations in the early universe which were larger than the particle horizon when energy density fell below that of an electron per Compton volume should therefore have been safe from dissipation.

This provides a conservative lower size bound of roughly  $10^3 km$ . If such configurations then simply tracked overall metric expansion, their corresponding minimum size today would be only  $\sim$  one light year.

By Eq. (2), the expected residual luminosity after  $n$  gradient crossings is  $\cos^{2n}(\theta_W) \simeq 0.77^n$ . If you assume domains one light year across and substitute the distance to the center of the Milky Way ( $\simeq 27000$  light years) or to the Andromeda galaxy ( $\simeq 2.6$  million light years) into this expression, the problem is obvious: we should not be able to see anything beyond the nearest stars!

Clearly, there is something wrong with this picture. The following exotic options have been on the table for years:

- The Higgs mechanism is not realized in nature (as Penrose suggested in [1]). Given the exasperatingly good agreement of the Standard Model with experiment, this alternative always faced very long odds. A confirmed discovery of one or more Higgs bosons at the LHC would just be the last nail in the coffin.
- The theory is *defined* by its perturbative expansion, while the electroweak Lagrangian and path integral are nothing more than convenient “book-keeping devices” used to aid in the construction and evaluation of Feynman diagrams [39]. If this is the case, non-perturbative structures like domain boundaries do not exist. There are both empirical and theoretical problems with this view. Empirically, a discretization of the full, non-perturbative path integral works very well for QCD [40], which raises the question why it should not work for electroweak interactions. Theoretically, the perturbation series is not guaranteed to converge (in the simple case of QED it has long been understood to diverge [41]). The closest well-defined object would be a sum over a finite number of terms, which is hard to accept as more than an ad-hoc computational device.
- Inflation ends at or below the electroweak scale, so the entire observable universe fits within one electroweak domain (or a few, just big enough to fit SNe Ia data). Several models of Higgs-mediated inflation which could produce this result have been proposed in recent years (see [42]-[45] and references therein).

If these were the only alternatives, the choice would be easy. Having the Higgs field do double duty as the inflaton through a non-minimal coupling to gravity is a particularly attractive idea. But before we jump to conclusions, we should remember that the end of dissipation does not imply the end of dynamics. Domains could keep growing by convective charge transport. There may not even be clearly identifiable domains, just a continuously varying  $\langle\Phi\rangle$  background where photon propagation becomes a more complicated problem. The distribution

of  $\langle\Phi\rangle$  on its vacuum manifold could be non-uniform, since the  $O(4)$  symmetry of the latter is larger than the  $SU(2)\times U(1)$  symmetry of electroweak interactions.

To find out, one must tackle the non-linear dynamics of electroweak theory in the low energy limit.

## II. NON-LINEAR SIGMA MODEL

When  $\langle\Phi\rangle$  is constrained to its vacuum manifold using polar field coordinates  $\vec{\theta} = [\theta_1, \theta_2, \theta_3] \in [-2\pi, 2\pi]$  and all massive gauge bosons are set to zero, the boson sector of the standard electroweak Lagrangian reduces to

$$\begin{aligned} \mathcal{L} = & \frac{1}{2} G_{ab} \partial_\mu \theta^a \partial^\mu \theta^b \\ & + \frac{1}{2} \partial_\mu A_\nu (\partial^\nu A^\mu - \partial^\mu A^\nu) \\ & + \frac{1}{2} H_{ab} A_\mu \partial_\nu \theta^a (A^\nu \partial^\mu \theta^b - A^\mu \partial^\nu \theta^b) \end{aligned} \quad (3)$$

where  $G_{ab}$  is the 3-sphere metric, Eq. (C24),  $H_{ab}$  is its counterpart on the vacuum manifold of the gauge bosons, Eq. (C22), and the scale parameter  $\nu$  has been absorbed into the photon field  $A_\mu$  (see Appendix C).  $G_{ab}$  and  $H_{ab}$  only depend on  $\vec{\theta}$ , not on its derivatives or on  $A_\mu$ .

To leading order, this is the effective Lagrangian of the standard electroweak model in the low energy, long distance limit. It consists of the  $O(4)$  non-linear sigma model (NSLM; the first line) coupled to electromagnetism (the second line) by an effective photon mass term (the third line) which is non-zero only when  $\vec{\theta}$  is not constant. It remains physically valid at least as long as the resulting energy density stays below the pair production threshold for the lightest weakly interacting particle. Excluding unknowns, that means an electron neutrino, with mass currently estimated to be somewhere in the range  $m_\nu \simeq 0.1 - 1 eV$ . Efficient production of a neutrino pair requires an energy of at least  $2m_\nu$  within the Compton volume  $1/m_\nu^3$  of a neutrino, i.e. an energy density  $> 2m_\nu^4 \simeq 2(0.1 - 1 eV)^4$ . As a comparison, the current dark energy density is estimated to be  $\simeq (3 \cdot 10^{-3} eV)^4$ .

It is a straightforward exercise to derive equations of motion from  $\mathcal{L}$ . They are messy, but some things can be learned from them by inspection. Since all couplings between  $\vec{A}$  and  $\vec{\theta}$  are through derivative terms, it is clear that making  $\vec{\theta}$  constant decouples it. On a flat, static  $\vec{\theta}$  background, all we will ever have is plain electromagnetism; without an initial “dent” in  $\vec{\theta}$  to give  $\vec{A}$  traction, there is nothing  $\vec{A}$  can do to push  $\vec{\theta}$  around. Likewise,  $\vec{A} = 0$  leaves us with the plain NLSM and its known special solutions (including, in particular, plane waves).

The  $O(4)$  NLSM has long been a popular toy model of domain formation and growth. On a lattice, its ground state is known to undergo a transition from disordered to ordered when the coupling encoded by  $G_{ab}$  exceeds a threshold value [46]. Since that coupling is inversely

proportional to spatial scale, this implies long-range disorder and short-range order, i.e. a domain structure, independently of particle horizons or other cosmological considerations. Its dynamics after a quench from a disordered, high temperature state has also been studied extensively in the context of condensed matter [47]. An elementary but important insight from these works is that relaxation time diverges with system size, so an infinite system never reaches a final, static equilibrium. Instead, a scaling state emerges, characterized by an average domain size  $L$  which typically grows as some power of time  $t$ . Models with non-conserved order parameters, like the  $O(4)$  NLSM, feature domain sizes  $L \propto \sqrt{t}$ .

It is easy to see that domain growth is not compatible with conservation of energy at domain boundaries in the plain NLSM: energy in a given volume is proportional to domain boundary area  $\propto L^2$ , the number of domains is  $\propto 1/L^3$ , so total energy is  $\propto 1/L$ . Unless something causes surface energy density at the boundaries to grow  $\propto L$  (boundary width shrinking?) energy must be lost to the environment as domains grow. Absent couplings to other fields, as is effectively the case when we set  $A_\mu = 0$  in  $\mathcal{L}$ , we can therefore not expect to observe domain growth (in Minkowski space; on the FRW metric, gradient energy can be siphoned off by the expansion of space). The dynamics is then best understood in terms of colliding wavefronts which quickly break up and lose their memory of initial conditions. Since  $\mathcal{L}$  is rotationally invariant both in coordinate and inner space, we should expect the end state to be a thermal distribution of isotropic  $\vec{\theta}$  radiation. This is confirmed by numerical simulations. Visualizations of energy density in such simulations are reminiscent of a room filling with smoke, reflecting the breakup of initial wavefronts into smaller ones.

What happens when  $\vec{A} \neq 0$ ?

In the time-axial gauge  $A_0 = 0$ , the mixed energy density terms (see Eq. (C23))

$$\begin{aligned} & \frac{1}{2} (\partial_0 \vec{\theta})^T \mathbb{H} (\partial_0 \vec{\theta}) A_m A_m \\ & + \frac{1}{2} (\varepsilon_{jkl} A_k \partial_l \vec{\theta})^T \mathbb{H} (\varepsilon_{jmn} A_m \partial_n \vec{\theta}) \end{aligned} \quad (4)$$

can be rearranged as the quadratic form  $\frac{1}{2} \vec{A}^T \mathbb{M} \vec{A}$ , where the  $3 \times 3$  matrix  $\mathbb{M}$  has components

$$M_{11} = \left( \partial_0 \vec{\theta}^T \mathbb{H} \partial_0 \vec{\theta} + \partial_2 \vec{\theta}^T \mathbb{H} \partial_2 \vec{\theta} + \partial_3 \vec{\theta}^T \mathbb{H} \partial_3 \vec{\theta} \right) \quad (5)$$

$$M_{22} = \left( \partial_0 \vec{\theta}^T \mathbb{H} \partial_0 \vec{\theta} + \partial_1 \vec{\theta}^T \mathbb{H} \partial_1 \vec{\theta} + \partial_3 \vec{\theta}^T \mathbb{H} \partial_3 \vec{\theta} \right) \quad (6)$$

$$M_{33} = \left( \partial_0 \vec{\theta}^T \mathbb{H} \partial_0 \vec{\theta} + \partial_1 \vec{\theta}^T \mathbb{H} \partial_1 \vec{\theta} + \partial_2 \vec{\theta}^T \mathbb{H} \partial_2 \vec{\theta} \right) \quad (7)$$

$$M_{12} = \left( -\partial_2 \vec{\theta}^T \mathbb{H} \partial_1 \vec{\theta} \right) \quad (8)$$

$$M_{13} = \left( -\partial_3 \vec{\theta}^T \mathbb{H} \partial_1 \vec{\theta} \right) \quad (9)$$

$$M_{23} = \left( -\partial_3 \vec{\theta}^T \mathbb{H} \partial_2 \vec{\theta} \right) \quad (10)$$

Since  $\mathbb{H}$  is real and symmetric,  $\mathbb{M}$  is too, and can therefore always be diagonalized. Its three eigenvalues are the

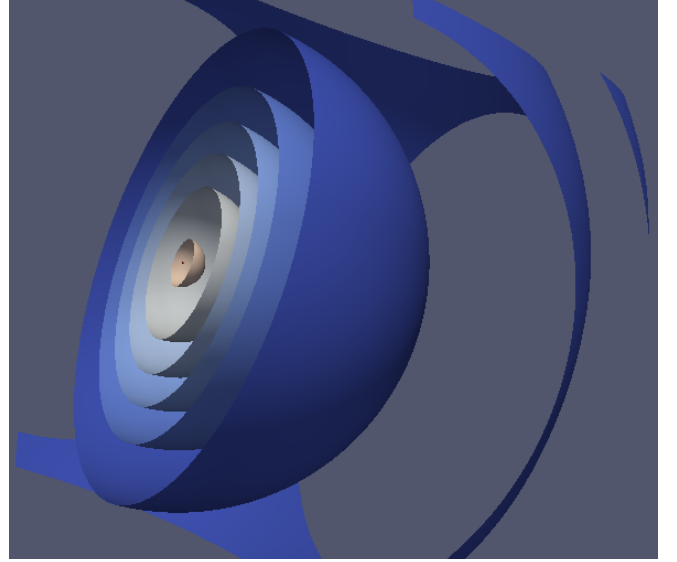


FIG. 1: Middle eigenvalue of  $\mathbb{H}$ , cut through isosurfaces from 0.01 to 0.4 (bluer is smaller) centered on  $\vec{\theta} = 0$ .

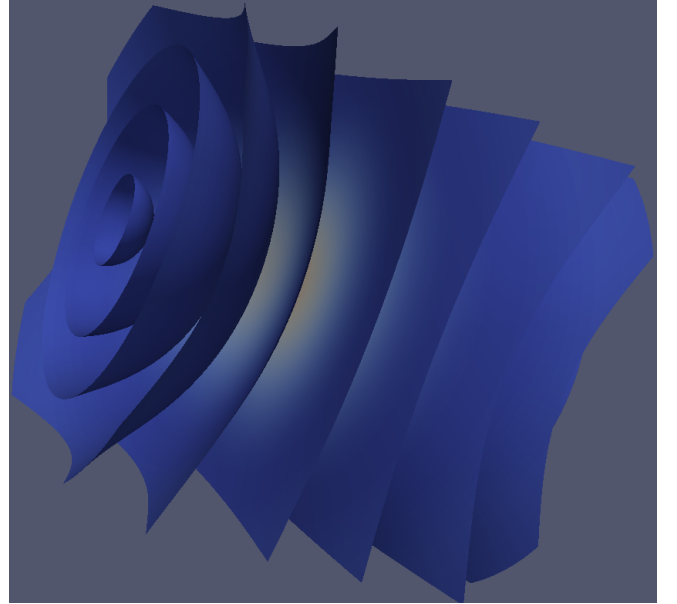


FIG. 2: High eigenvalue of  $\mathbb{H}$ , isosurfaces from 0.01 to 0.4 (bluer is smaller). The symmetry axis is  $\theta_3$ .

squared effective masses of the photon in the three principal directions defined by its eigenvectors. As  $\vec{\theta}$  derivatives grow larger, so does the effective photon mass.

A numerical exploration of  $\mathbb{H}$  reveals that unlike  $\mathbb{G}$ , it is highly anisotropic. While it always has at least one vanishing eigenvalue for any  $\vec{\theta}$ , its middle eigenvalue peaks at  $\theta = 0$  and falls off for larger  $\theta$ . Its largest eigenvalue is symmetric about the line  $\theta_1 = \theta_2 = 0$  and antisymmetric along it. On that line, the only non-zero elements of  $\mathbb{H}$

are

$$H_{11} = H_{22} = 2 \sin^2(\theta_W) \theta_3 (1 - \cos(\theta_3)) \quad (11)$$

with peaks and troughs at  $\theta_3 \simeq \pm 3.67$ . In  $\mathbb{M}$ , these elements only multiply derivatives of  $\theta_1$  and  $\theta_2$ , so the effective photon mass vanishes not only for constant  $\vec{\theta}$ , but also everywhere on the line  $\theta_1 = \theta_2 = 0$ .

This is not surprising if you follow the derivation of  $\mathcal{L}$  in Appendix C. The auxiliary quantities  $\Theta_1$  and  $\Theta_2$  of Eqs. (C7) and (C8) are essentially the Goldstone bosons associated with the electrically charged  $W^\pm$  bosons, while the  $\Theta_3$  of Eq. (C9) is associated with the electrically neutral  $Z^0$  boson.  $\mathbb{M}$  vanishes when  $\theta_1 = \theta_2 = 0 \Rightarrow \Theta_1 = \Theta_2 = 0$  because the photon does not interact directly with electrically neutral fields.

Physically, the decoupling of  $\vec{\theta}$  and  $\vec{A}$  along  $\theta_1 = \theta_2 = 0$  suggests that  $\vec{\theta}$  will be driven to that line by electromagnetic radiation, essentially because it will be kicked around randomly until it happens to land there. The simplest way to make this conclusion at least mathematically plausible is to look for minima in the speed  $s = |\partial_0(\vec{\theta}, \vec{\Pi})|$  of the Hamiltonian phase space flow  $\partial_0(\vec{\theta}, \vec{\Pi}) = (\partial H / \partial \vec{\Pi}, -\partial H / \partial \vec{\theta})$ , or equivalently in

$$s^2 = \frac{\partial H}{\partial \Pi_a} \frac{\partial H}{\partial \Pi_a} + \frac{\partial H}{\partial \theta_a} \frac{\partial H}{\partial \theta_a} \quad (12)$$

In general, finding such minima is hard work, but if we also require that  $\nabla \theta_a = \vec{\Pi} = 0$  (i.e. constant, static configurations, as expected for global energy minima), the only non-vanishing second derivatives of the Hamiltonian are

$$\frac{\partial^2 H}{\partial \Pi_a \partial \Pi_b} = [\mathbb{K}^{-1}]_{ab} \quad (13)$$

where

$$\mathbb{K} = \mathbb{G} + \vec{A}^2 \mathbb{H} \quad (14)$$

Since minima of  $s^2$  should have vanishing derivatives in  $\vec{\theta}$  and  $\vec{\Pi}$ , the minima of the largest eigenvalue of  $\mathbb{K}^{-1}$  should roughly coincide with the  $\vec{\theta}$  least susceptible to being kicked around by  $\vec{A}$ . For  $\vec{A}^2 = 0$ , the largest eigenvalue at  $\vec{\theta} = 0$  is 4; from there, it grows isotropically with  $|\vec{\theta}|$ . For finite  $\vec{A}^2$ , the minimum is still 4 at  $\vec{\theta} = 0$ , but larger values form concentric prolate spheroids extending along the  $\theta_3$  axis.

It is therefore reasonable to expect the system to end up spending most of its time around that axis, i.e. around the line  $\theta_1 = \theta_2 = 0$ .

### III. HANLON

Beyond the simplest cases (essentially constant fields and traveling waves) the exploration of  $\mathcal{L}$  requires numerical integration of the equations of motion. Several software packages geared towards field-theoretic simulations

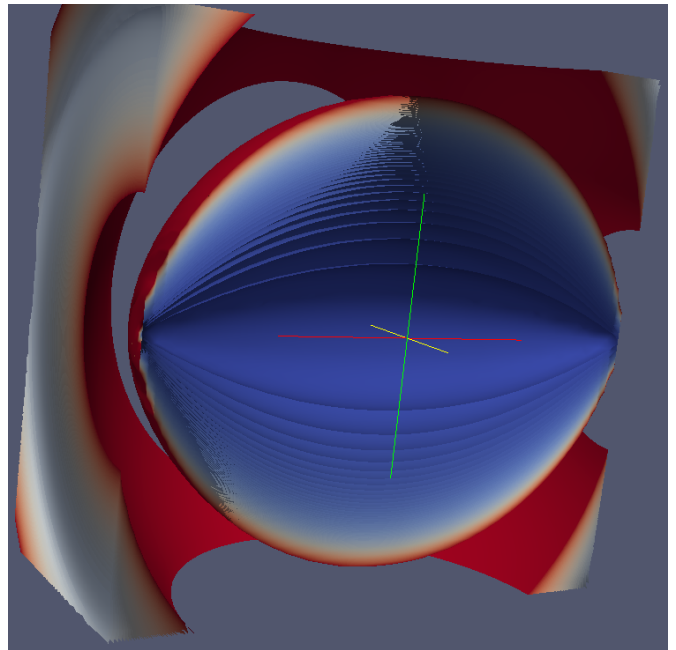


FIG. 3: Max eigenvalues of  $\mathbb{K}^{-1}$  with  $\vec{A}^2 = 100^2$ : cut through isosurfaces for levels 5, 6, ..., 100. The red line is the  $\theta_3$  axis.

in the early universe have been developed over the years (e.g. [48]-[51]) but none capable of handling the non-linear vector-scalar interaction terms of  $\mathcal{L}$ . A dedicated set of programs, dubbed HaNLON (for Hamiltonian Non-Linear Open Numerics, and the eponymous razor) was therefore developed for this purpose. Its centerpiece is a symplectic integrator based on the Störmer-Verlet algorithm (SV; see [52] for a review) applied to a discretized Hamiltonian derived from  $\mathcal{L}$ . The algorithm allows long runs without significant energy drift, and an improved fourth order stencil ensures that any anisotropies introduced by the discretization do not occur until sixth order [53]. On a  $64^3$  point lattice, this means relative discretization errors are  $\mathcal{O}(10^{-8})$ , while anisotropies are at least a factor  $1/64^2 \simeq 2 \cdot 10^{-4}$  smaller. Double precision arithmetic is used throughout.

Details of the implementation are discussed elsewhere [54].

All simulations reported in this paper were carried out on a  $64^3$  point lattice with periodic boundary conditions using an Intel Core i7-2600K CPU overclocked to  $5.8 GHz$ . The shortest run took five days, the longest three months. Additional materials, including animations of the evolution of various quantities, are available online [55].

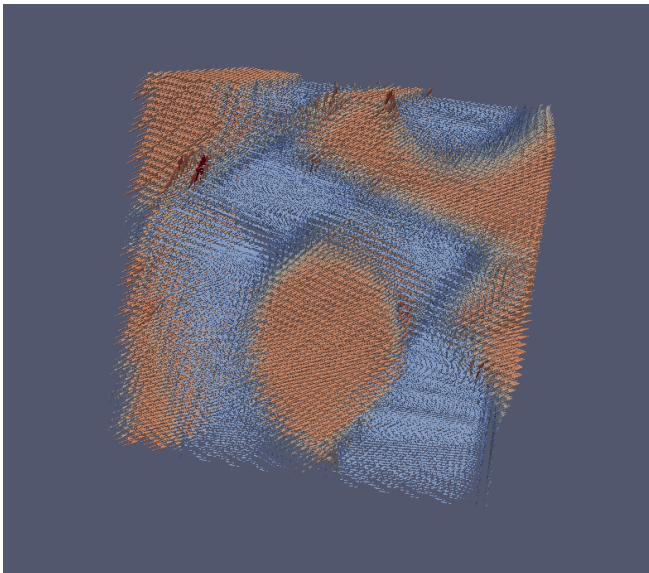


FIG. 4: An initial  $\vec{\theta}$  configuration chosen for ease of visualization. Domains with two different values of  $\vec{\theta}$  extend along one spatial axis.

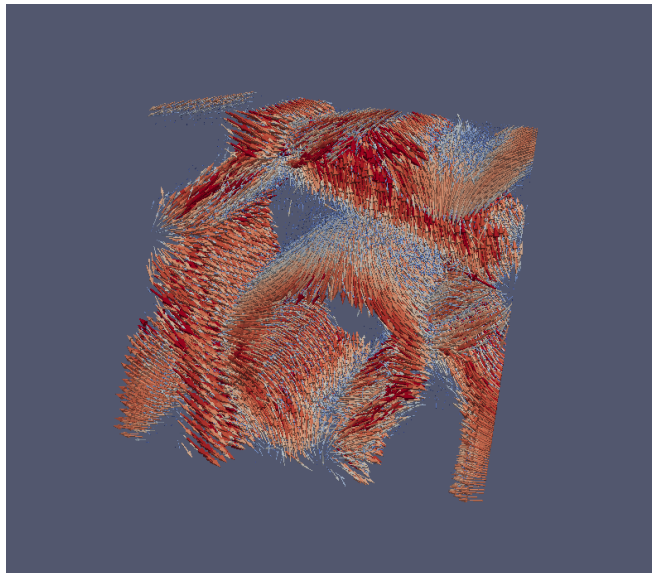


FIG. 6: Magnetic fields around the  $\vec{\theta}$  domain boundaries of Fig. 4. Color encodes  $|\vec{B}|$  (red is larger).

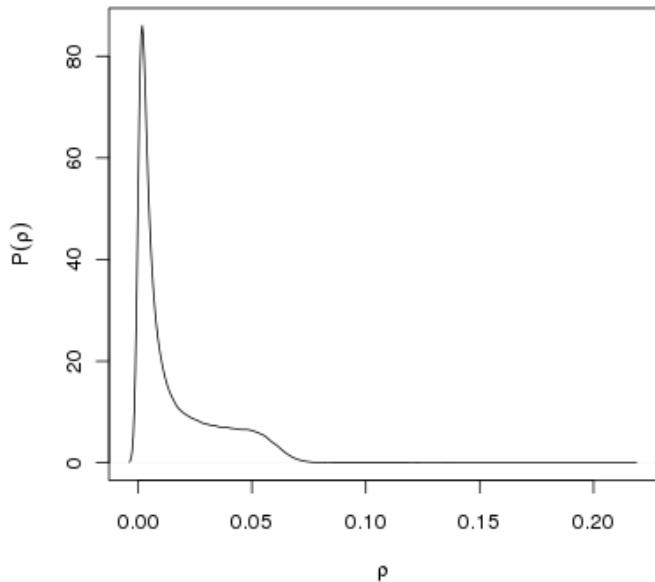


FIG. 5: NLSM, initial energy distribution.

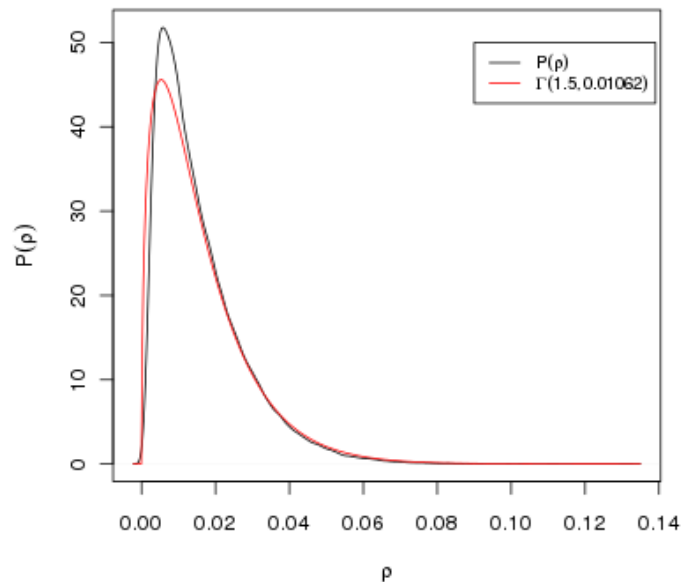


FIG. 7: NLSM, energy distribution at  $t = 64$  and best  $\Gamma(1.5, 1/\beta)$  fit.

## IV. MINKOWSKI SPACE

### A. NLSM vs EFT

Both the dimming problem which motivated this work and its possible dynamic resolution are well illustrated by two simulations in Minkowski space starting from similar initial conditions.

In the first simulation (12 days of wall time using a fixed time step of  $10^{-4}$  lattice time units), the initial  $\vec{\theta}$  configuration is similar to that of Fig. 4, i.e. domains

with two different values of  $\vec{\theta}$  extending along one spatial axis. It was obtained by local energy minimization of the same random seed used to produce the configuration of Fig. 4, but with  $\vec{A}$  clamped to 0.  $\vec{A} = 0$  is conserved by the equations of motion, so the resulting dynamics is that of the plain  $O(4)$  NLSM. Binning lattice sites by energy yields an initial distribution sharply peaked near zero (corresponding to the bulk of the domains), with a smaller bump for the boundaries (Fig. 5).

When the clock starts ticking, each domain boundary



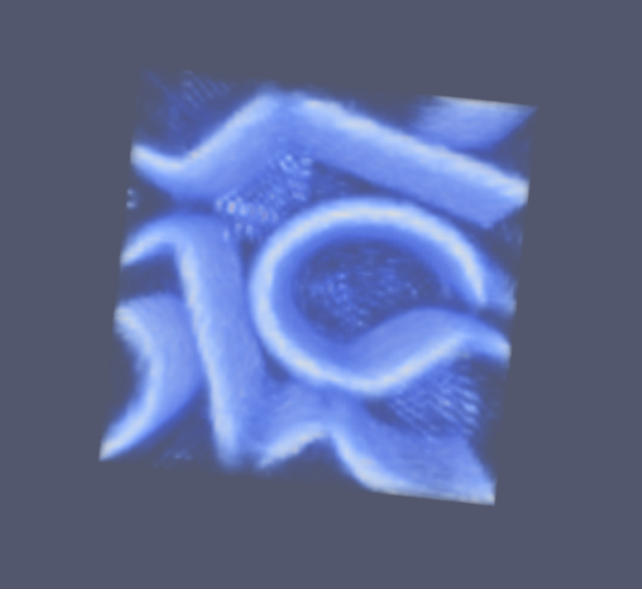


FIG. 8: NLSM, initial energy density.

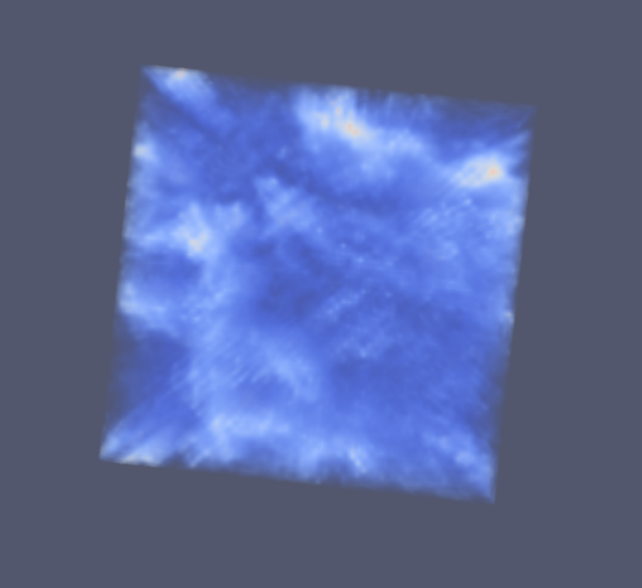


FIG. 9: NLSM, energy density at  $t = 64$ .

immediately splits into twin wavefronts moving in opposite directions, and collisions ensue.

Halfway through the simulation, at 32 lattice time units, wavefronts start colliding with the replicas from neighboring simulation cubes which are implied by the periodic boundary conditions. Extending the simulation into this “unphysical” regime is justified *a posteriori* by the observed loss of information. The initial wavefronts break up as space is filled with a disordered “smoke” of smaller waves, and the energy distribution at the end of the simulation approaches the familiar  $\Gamma(1.5, 1/\beta)$ , i.e. Maxwell-Boltzmann, shape of a thermalized system (Fig. 7).

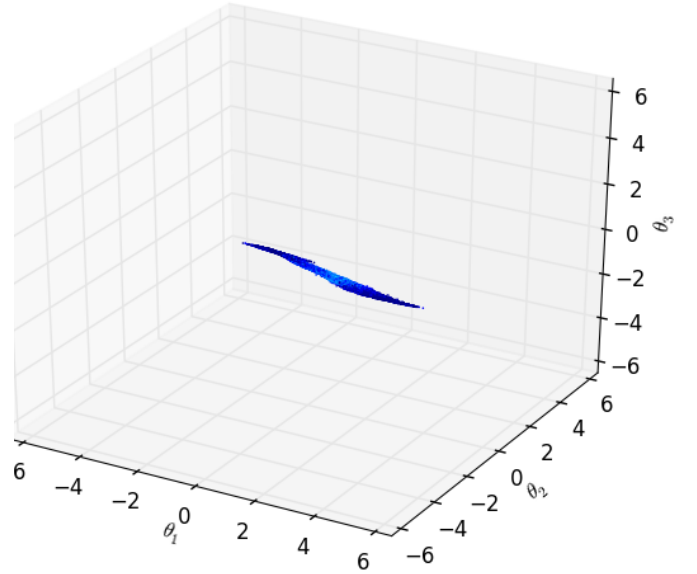


FIG. 10: NLSM, scatter plot of initial  $\vec{\theta}$ .

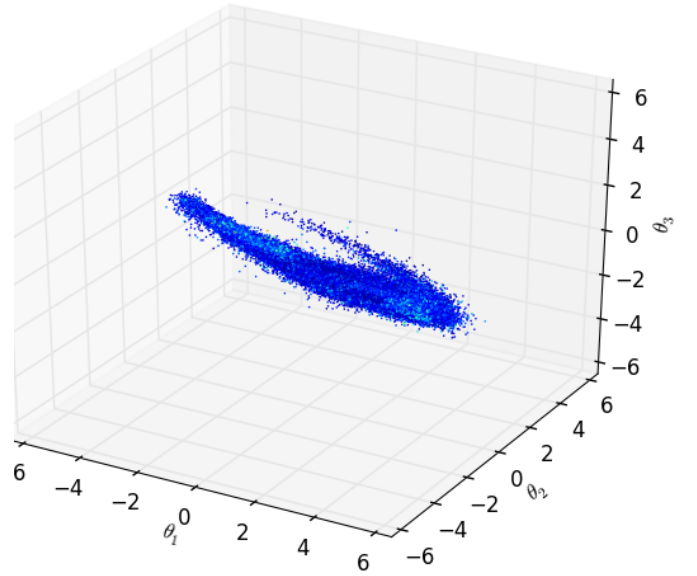


FIG. 11: NLSM, scatter plot of  $\vec{\theta}$  at  $t = 64$ .

The initial  $\vec{\theta}$  distribution is aligned with the  $\theta_1$  axis, and although it spreads out over time, the overall orientation is roughly preserved throughout the simulation. The average normalized  $\vec{\theta}$  components display no significant trend, as expected given the absence of a preferred direction (Figs. 10-12).

Average photon mass eigenvalues, on the other hand, grow over time, consistent with an evolution toward shorter  $\vec{\theta}$  wavelengths (Fig. 13). If this trend were to carry over to the general case with  $\vec{A} \neq 0$ , the universe would become increasingly opaque as time goes by.

In the second run, the starting point is the configura-

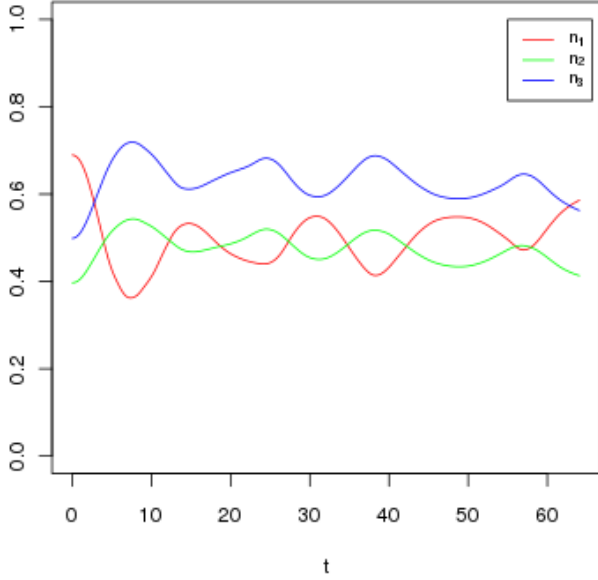


FIG. 12: NLSM, evolution of average  $n_a = |\theta_a|/|\vec{\theta}|$ .

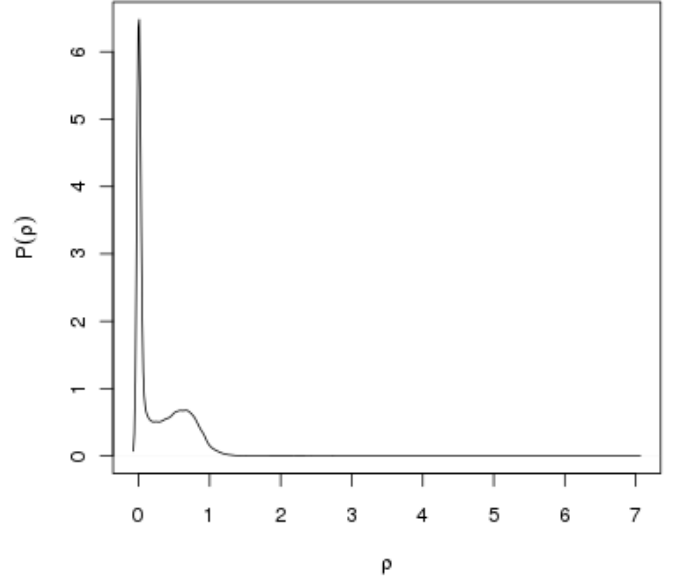


FIG. 14: EFT, initial energy distribution.

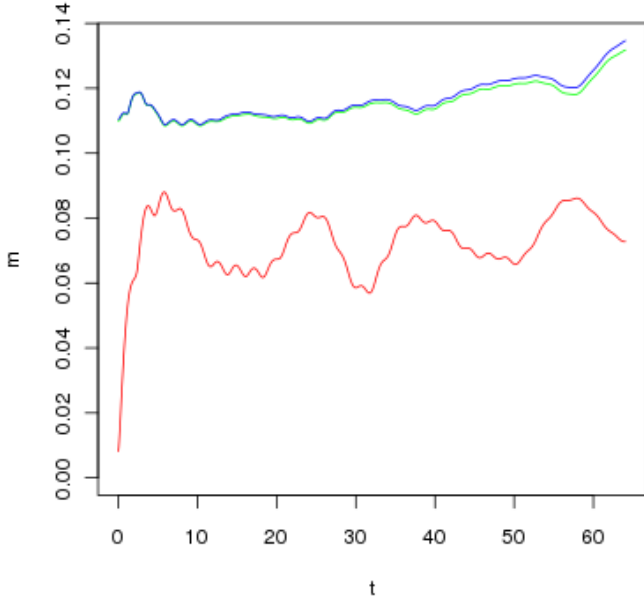


FIG. 13: NLSM, evolution of average photon mass eigenvalues.

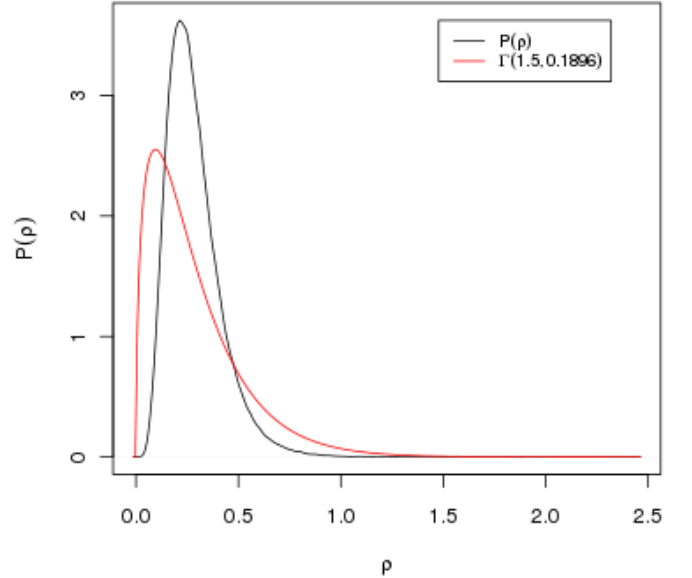


FIG. 15: EFT, energy distribution at  $t = 64$  and best  $\Gamma(1.5, 1/\beta)$  fit.

tion of Fig. 4.  $\vec{A} \neq 0$ , so the dynamics is that of the full low energy effective field theory (EFT). Most energy initially resides in the magnetic fields at the domain boundaries. Apart from a sharper secondary bump due to this additional contribution, the initial energy distribution is similar to the previous one (Fig. 14). When the simulation starts, the electric component quickly builds up as electromagnetic waves start propagating, while little energy is transferred to  $\vec{\theta}$  (Fig. 16).

Homogenization of the initial wavefronts proceeds visibly faster than in the NLSM case (incidentally, the faster

dispersion allows the use of a longer time step,  $10^{-3}$  lattice time units, for five days of wall time). The final energy distribution does not quite look thermal (Fig. 15), but the distributions for the separate components do (Figs. 17-19). They just have different temperatures.

This is consistent with the anticipated decoupling, which can be seen directly in the evolution of  $\vec{\theta}$ . As in the NLSM run, the initial distribution is aligned with the  $\theta_1$  axis, but by the end of the simulation, it has flipped over to the  $\theta_3$  axis (Figs. 20-22).

Decoupling is also reflected by the evolution of photon



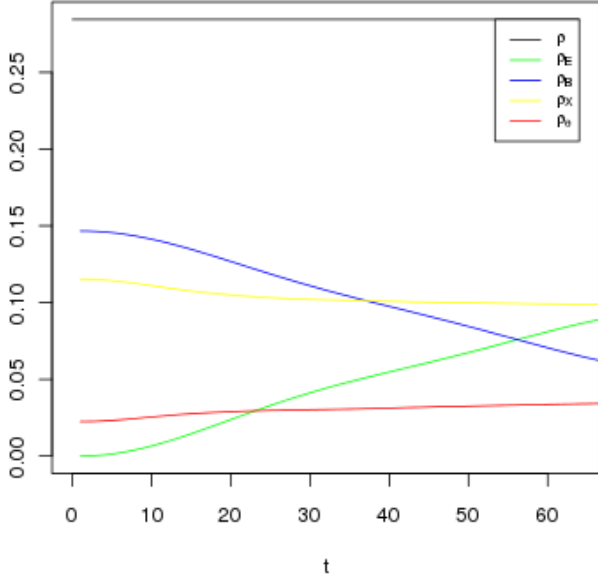


FIG. 16: EFT, evolution of contributions to total energy.

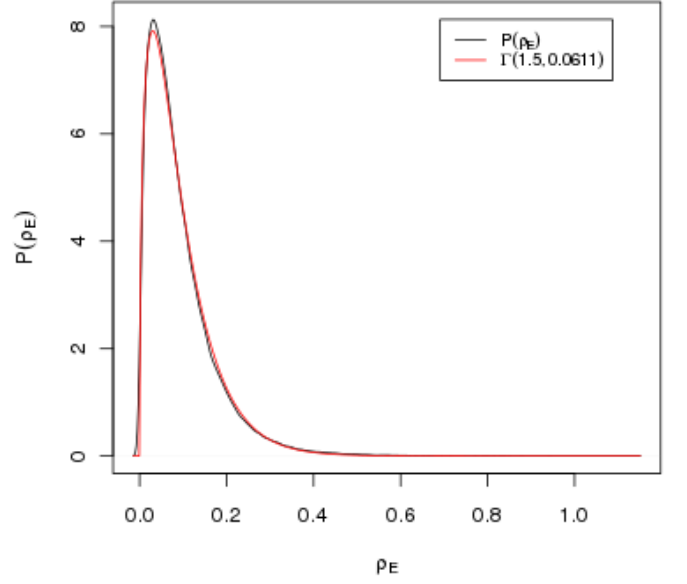


FIG. 18: EFT,  $\vec{E}$  energy distribution at  $t = 64$  and best  $\Gamma(1.5, 1/\beta)$  fit.

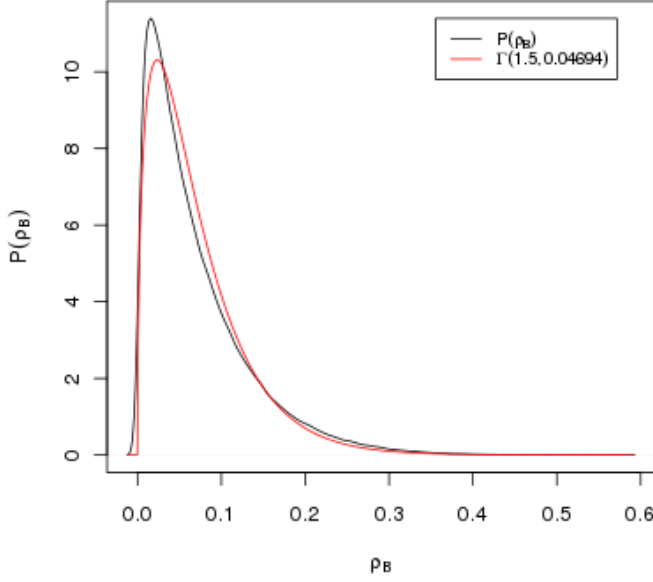


FIG. 17: EFT,  $\vec{B}$  energy distribution at  $t = 64$  and best  $\Gamma(1.5, 1/\beta)$  fit.

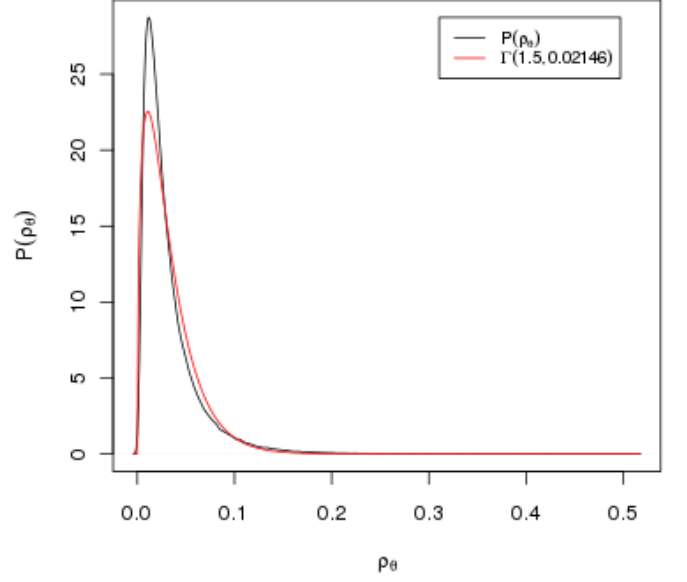


FIG. 19: EFT,  $\vec{\theta}$  energy distribution at  $t = 64$  and best  $\Gamma(1.5, 1/\beta)$  fit.

mass eigenvalues, which start declining after the initial jump caused by the acceleration of  $\vec{\theta}$  wavefronts from zero speed (Fig. 23).

In contrast to the plain NLSM case, the universe now becomes more transparent as time goes by.

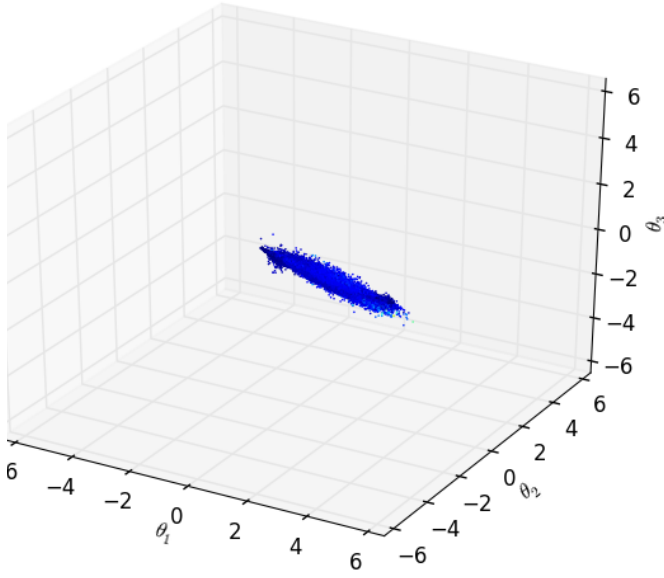
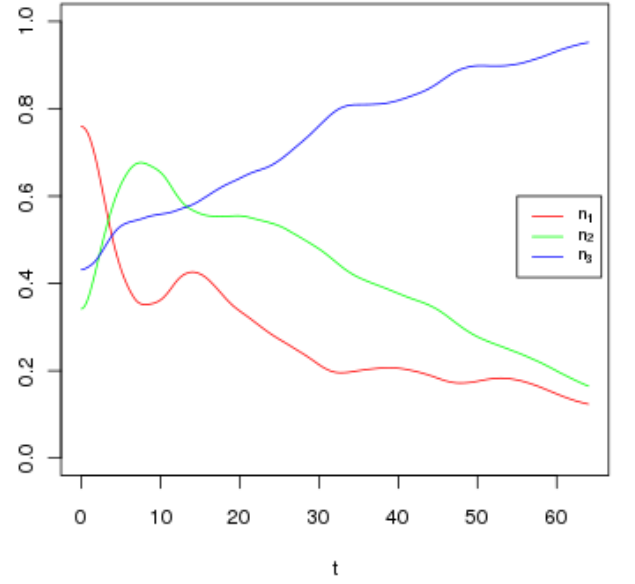
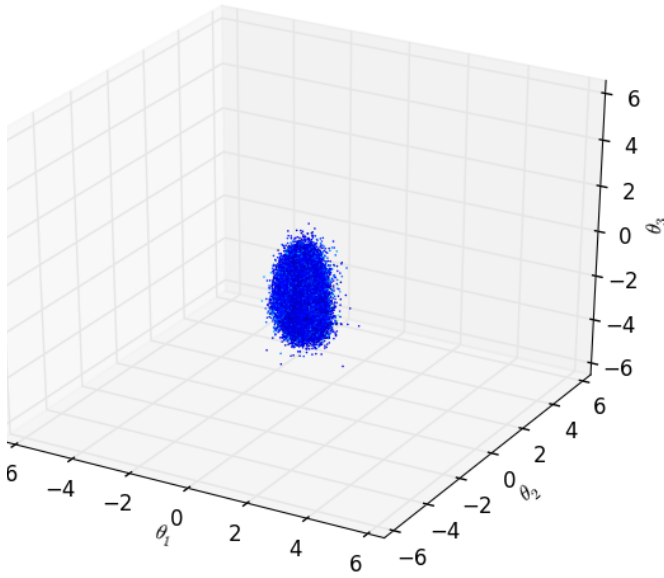
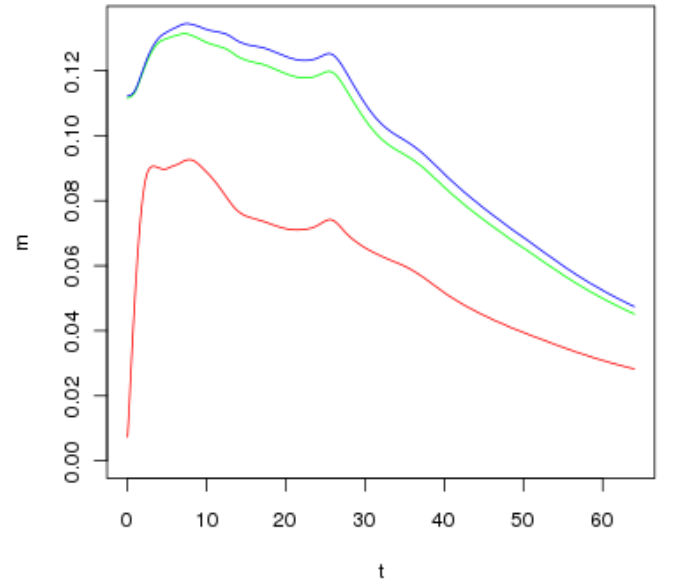
FIG. 20: EFT, scatter plot of initial  $\vec{\theta}$ .FIG. 22: EFT, evolution of average  $n_a = |\theta_a|/|\vec{\theta}|$ .FIG. 21: EFT, scatter plot of  $\vec{\theta}$  at  $t = 64$ .

FIG. 23: EFT, evolution of average photon mass eigenvalues.

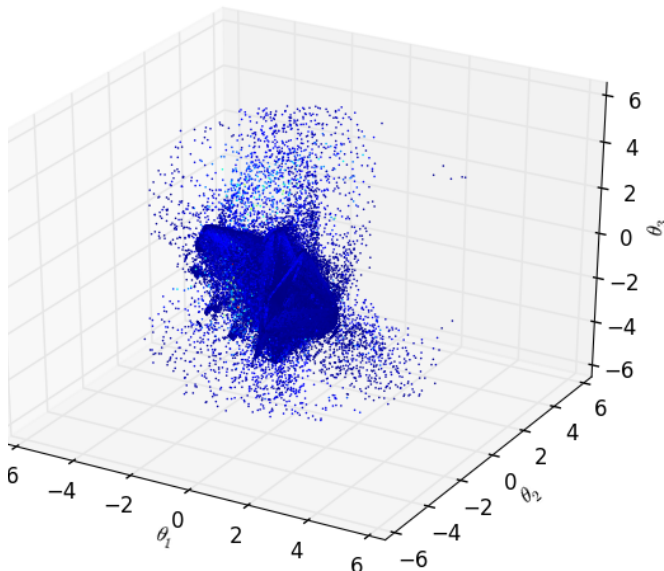


FIG. 24: Scatter plot of initial  $\vec{\theta}$ .

### B. $\vec{\theta}$ vs $\vec{B}$ energy

The EFT simulation of the previous section leaves room for some reasonable doubts. One is that the preference for the  $\theta_3$  axis displayed by  $\vec{\theta}$  might be caused by the anisotropy of the initial configuration. There is a preferred spatial axis and only a few dominant  $\vec{\theta}$  and  $\vec{A}$  directions. Another possibility is that the outcome might be qualitatively different if total energy were not strongly dominated by the electromagnetic field (roughly an order of magnitude larger than  $\vec{\theta}$  energy). Finally, the simulation did not run long enough to provide at least a strong hint about the ultimate fate of the effective photon mass. Does it fall all the way to zero, or does it level off at some finite value?

The first concern can be addressed by using more varied initial configurations, the second one by reducing electromagnetic energy density in successive runs, the third one by running each simulation longer.

For easier comparison between runs, it is convenient to use the same initial configuration and scale the  $\vec{B}$  field without minimizing energy density all over again (as that would change shapes and values of both  $\vec{\theta}$  and  $\vec{B}$ ). This increases the deviation from static equilibrium and is therefore likely to make the initial evolution somewhat faster, so strictly speaking it yields a lower bound on the time required to reach a given degree of homogenization,  $\vec{\theta}$  alignment or similar statistical measure.

Figs. 25-39 illustrate the evolution starting from

- an original configuration consisting of 10 true 3D Voronoi cells;
- the same configuration with the initial  $\vec{B}$  scaled by a factor 0.23571 to make its energy equal to that of

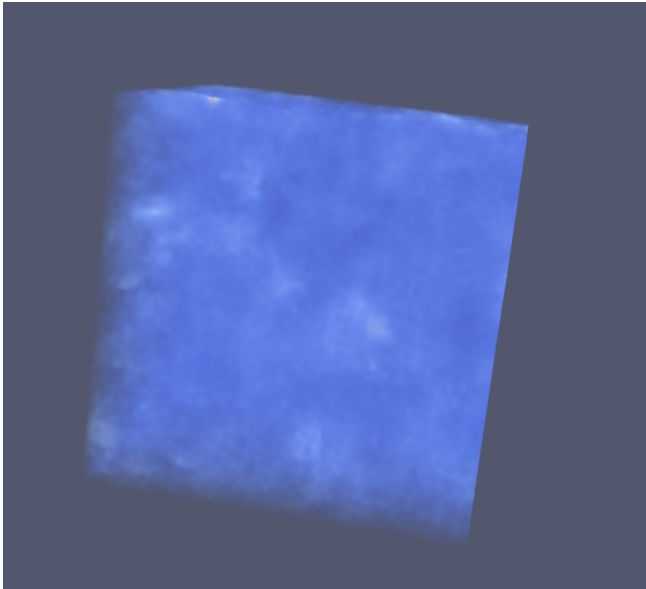
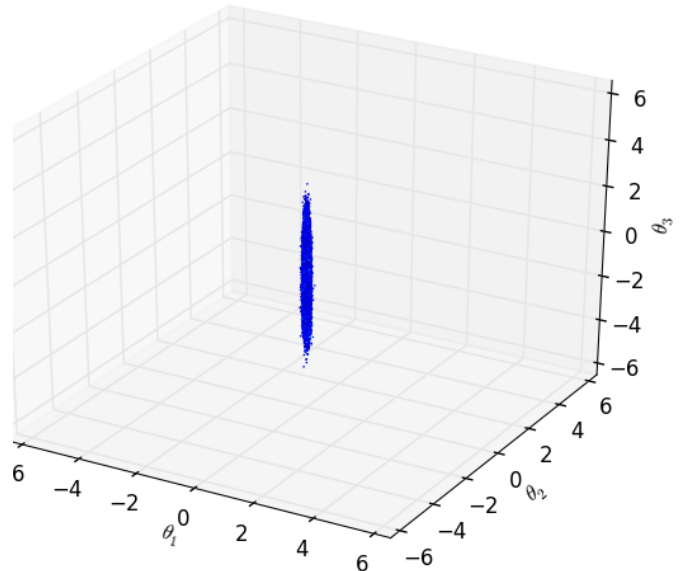
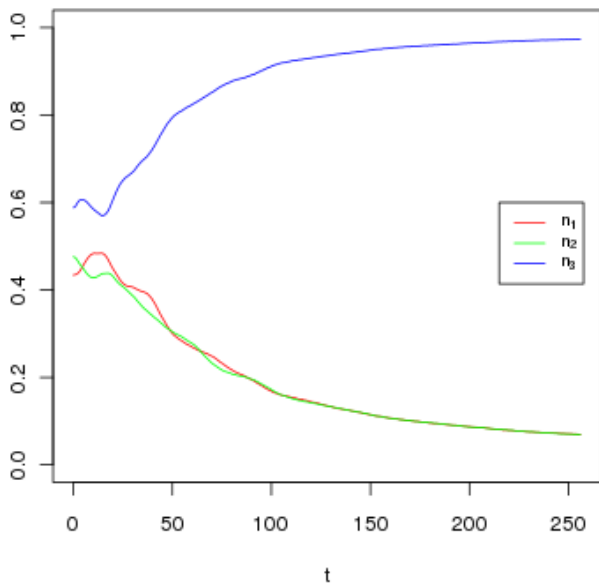
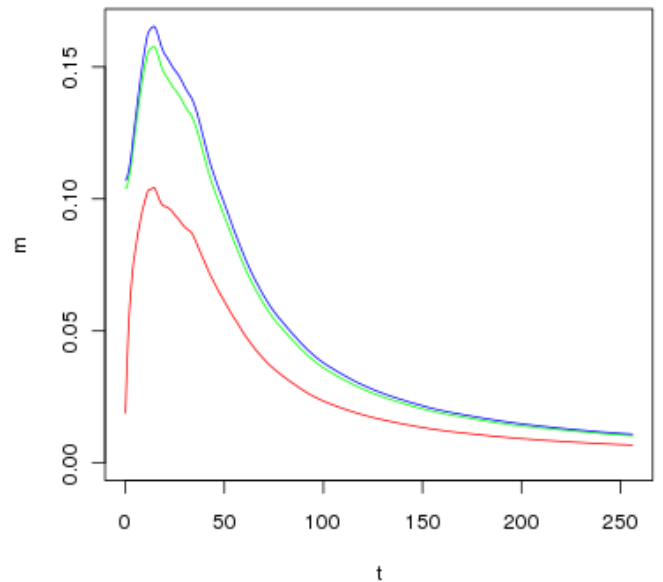
$\vec{\theta}$ ;

- the same configuration with the initial  $\vec{B}$  scaled by a factor 0.001.

The simulations took 12, 13 and 11 days of wall time, all with a fixed time step of  $10^{-3}$  lattice units.

As expected, reducing electromagnetic energy makes the  $\theta_3$  axis less attractive, and in the last case an offshoot along the  $\theta_1$  axis emerges halfway through the simulation, signaling the presence of electrically charged configurations. A visualization of energy density at the end of each simulation shows that less electromagnetic energy causes more numerous high density bubbles to form (Figs. 25, 29, 33). These are long-lived configurations which emerge 1/4 through the simulation and then remain essentially unchanged. They are primarily due to the  $\vec{E}$  and vector-scalar interaction energy terms, and also clearly discernible in visualizations of high and middle photon mass eigenvalues.

Average photon masses hold no surprises: first they rise as wavefronts accelerate, then they fall at a decelerating pace (Figs. 28, 32, 36). Their evolution strongly suggests an asymptotic leveling off at a non-zero value, as does the repartition of energy (Figs. 37, 38, 39).

FIG. 25: Original  $\vec{B}$ , energy density at  $t = 256$ .FIG. 27: Original  $\vec{B}$ , scatter plot of  $\vec{\theta}$  at  $t = 256$ .FIG. 26: Original  $\vec{B}$ , evolution of average  $n_a = |\theta_a|/|\vec{\theta}|$ .FIG. 28: Original  $\vec{B}$ , evolution of average photon mass eigenvalues.

Equipartition of energy does not seem to be in the cards. Inferred temperatures of the individual components remain different, and electric field energy grows to exceed magnetic field energy in all three cases. If electromagnetic energy were all radiation, this would not happen. The excess must be due to coherent electric fields, which again suggests the presence of electrically charged configurations.

Note how the swings in  $\vec{B}$  energy mirror those in  $\vec{E}$  energy (most clearly in Fig. 38). This strongly suggests the presence of plasma oscillations, i.e. periodically varying average separation between charges of opposite sign:

$\vec{E}$  energy peaks at the turning points, when the charges are momentarily standing still at maximum separation, while  $\vec{B}$  energy peaks when they are crossing at maximum speed.

Also note the increasing spikes in total and  $\vec{\theta}$  energy as  $\vec{B}$  is scaled down. Integration becomes harder as electromagnetic dissipation of  $\vec{\theta}$  configurations is reduced, but the algorithm manages to get back on track after minor events like this.

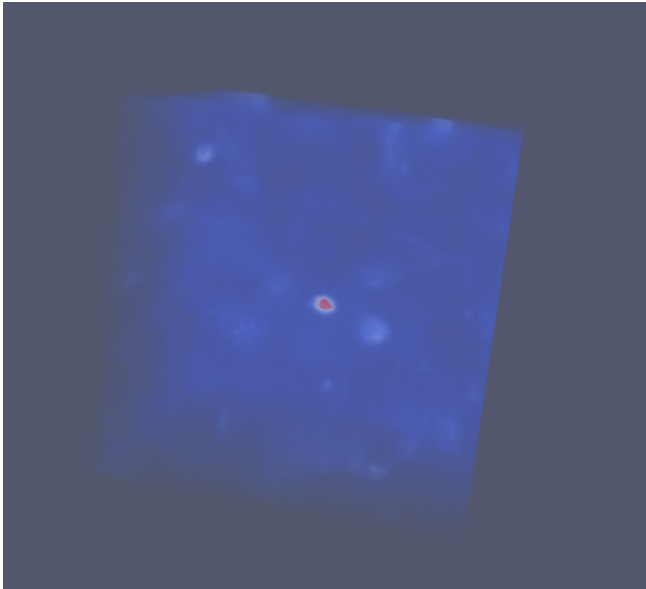


FIG. 29:  $\vec{B} \rightarrow 0.23571\vec{B}$ , energy density at  $t = 256$ .

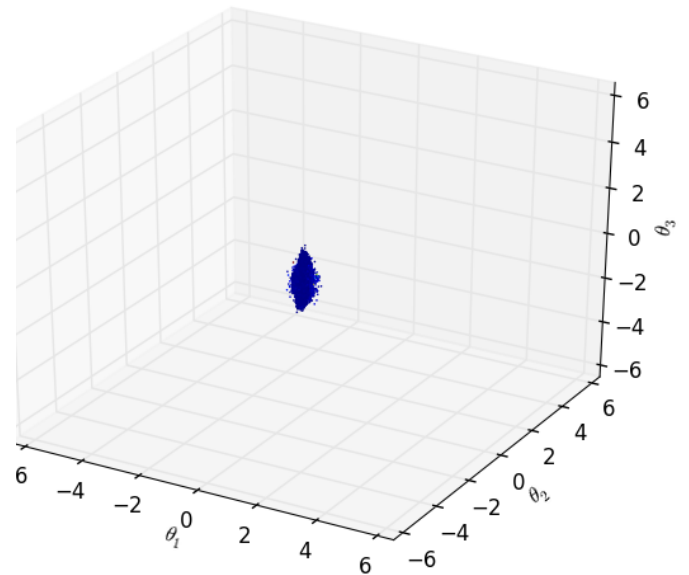


FIG. 31:  $\vec{B} \rightarrow 0.23571\vec{B}$ , scatter plot of  $\vec{\theta}$  at  $t = 256$ .

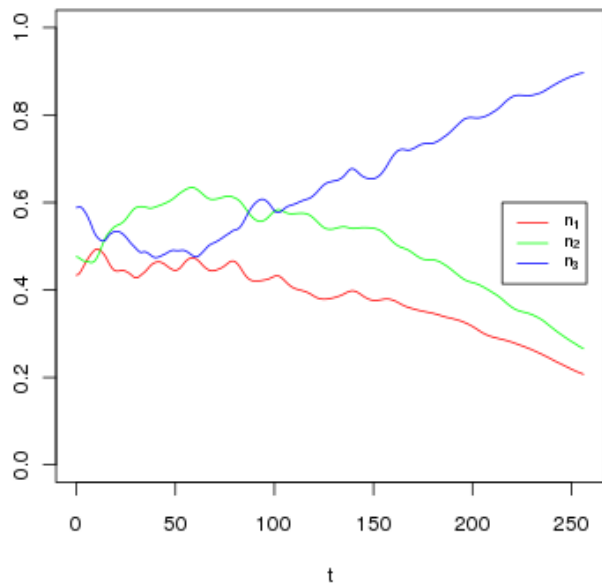


FIG. 30:  $\vec{B} \rightarrow 0.23571\vec{B}$ , evolution of average  $n_a = |\theta_a|/|\vec{\theta}|$ .

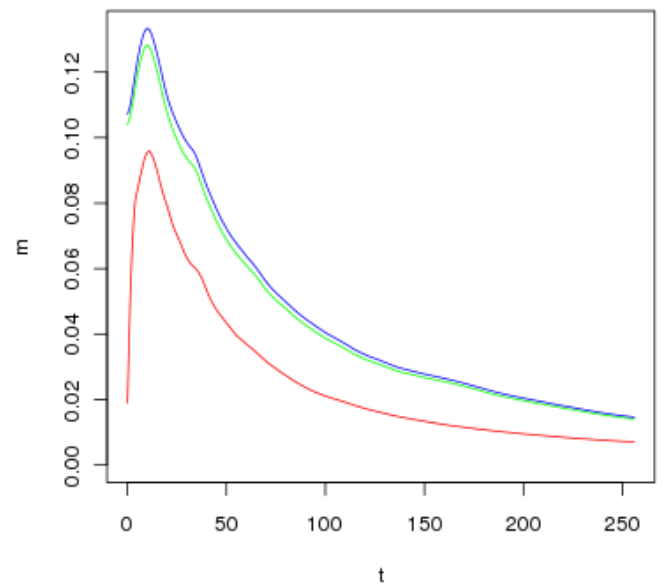


FIG. 32:  $\vec{B} \rightarrow 0.23571\vec{B}$ , evolution of average photon mass eigenvalues.

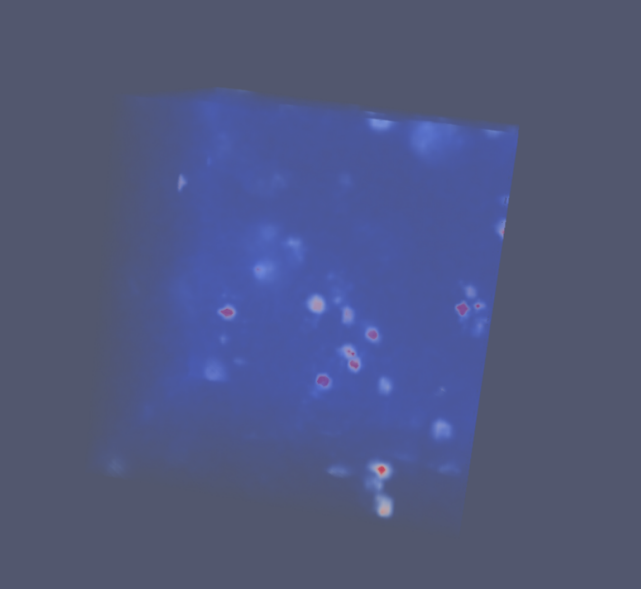


FIG. 33:  $\vec{B} \rightarrow 0.001\vec{B}$ , energy density at  $t = 256$ .

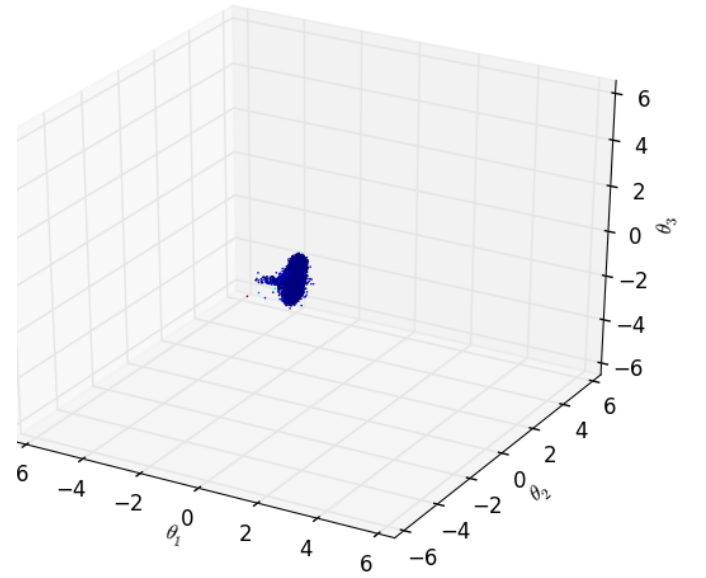


FIG. 35:  $\vec{B} \rightarrow 0.001\vec{B}$ , scatter plot of  $\vec{\theta}$  at  $t = 256$ .

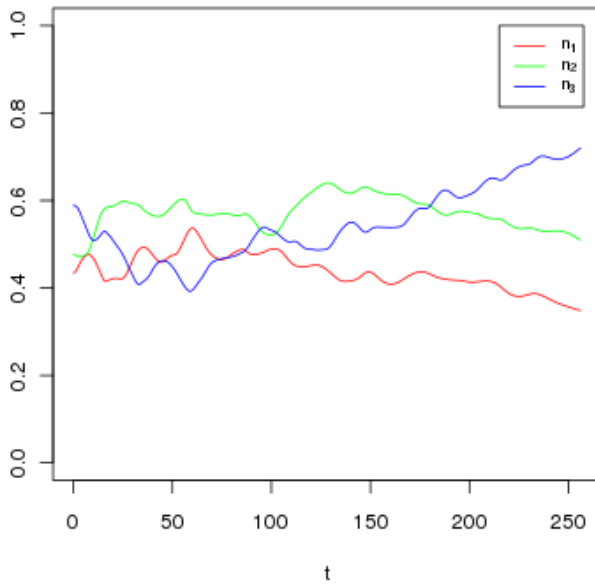


FIG. 34:  $\vec{B} \rightarrow 0.001\vec{B}$ , evolution of average  $n_a = |\theta_a|/|\vec{\theta}|$ .

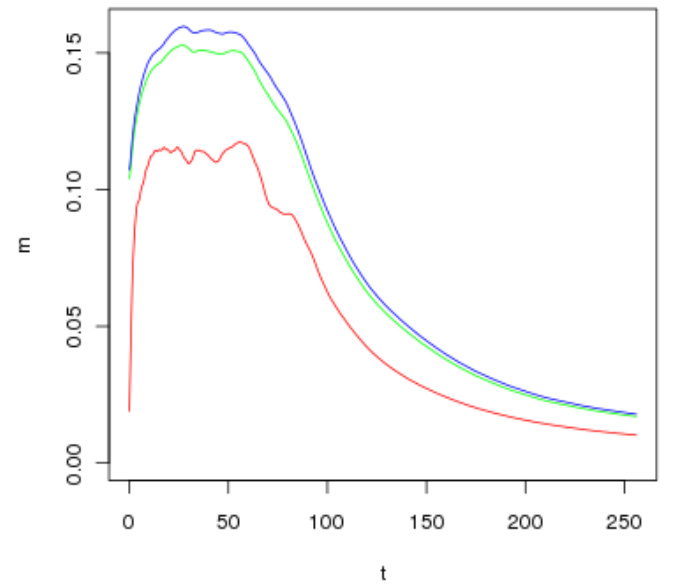


FIG. 36:  $\vec{B} \rightarrow 0.001\vec{B}$ , evolution of average photon mass eigenvalues.



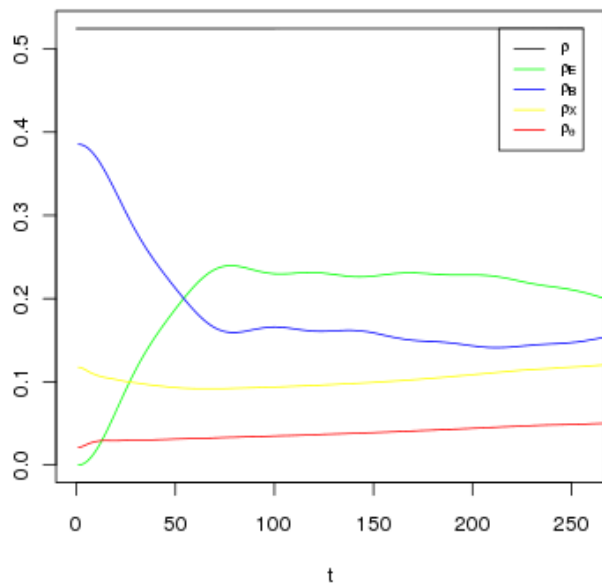


FIG. 37: Original  $\vec{B}$ , evolution of contributions to total energy.

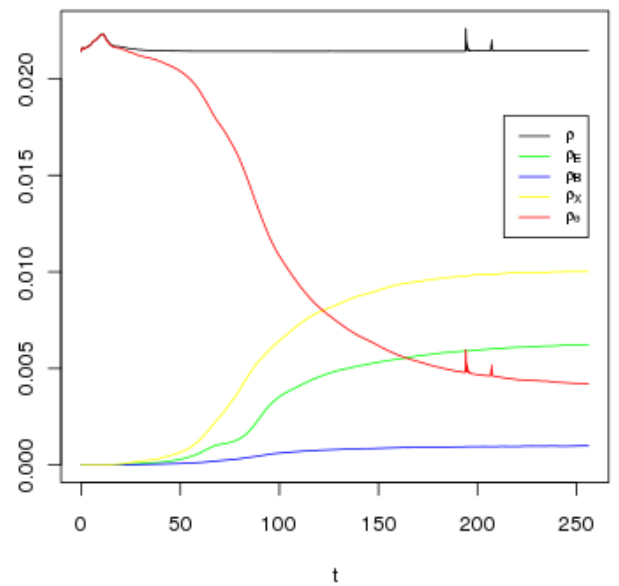


FIG. 39:  $\vec{B} \rightarrow 0.001\vec{B}$ , evolution of contributions to total energy.

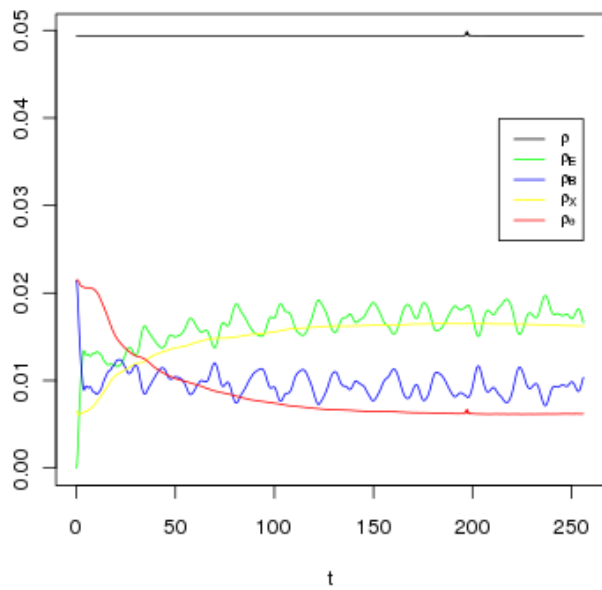


FIG. 38:  $\vec{B} \rightarrow 0.23571\vec{B}$ , evolution of contributions to total energy.

## V. FRW

### A. A problem of scale

The effect of going from Minkowski to FRW metric is evident by inspection of Eq. (D15): every  $\nabla$  and  $\vec{A}$  picks up a dimensionless scale factor  $1/a$ . It is convenient to introduce the same factor in time derivatives by a change of variable to conformal time (a.k.a. arc time)  $\eta$ , defined by

$$\frac{d\eta}{dt} = \frac{1}{a} \quad (15)$$

The time derivative of an arbitrary quantity  $f$  then becomes

$$\frac{df}{dt} = \frac{1}{a} \frac{df}{d\eta} \quad (16)$$

and the time elapsed since some reference time  $t = t_0 \Leftrightarrow \eta = 0$  is given by

$$t - t_0 = \int_0^\eta a(\eta) d\eta \quad (17)$$

The main advantage of conformal time is that a constant  $\eta$  interval maps to a  $t$  interval inversely proportional to  $a$ , so it is automatically adaptive: time runs faster closer to the bang, where dynamics is also faster.

In the full action integral, putting  $\mathcal{L}$  on the FRW metric introduces a volume factor  $\sqrt{-g} = a^3$ , and the change of variable to conformal time tacks on another factor  $a$ . When discussing spatial densities, it is natural to factor out the Jacobian for the time variable. Writing derivatives with respect to  $\eta$  as  $\partial_\eta$ , the spatial Lagrangian density, volume factor included, is then

$$\begin{aligned} \mathcal{L} = & \frac{a}{2} G_{lm} (\partial_\eta \theta^l \partial_\eta \theta^m - \nabla \theta^l \cdot \nabla \theta^m) \\ & + \frac{1}{2a} \left( (\partial_\eta \vec{A})^2 - (\nabla \times \vec{A})^2 \right) \\ & - \frac{1}{2a} H_{lm} (\vec{A} \times \nabla \theta^l) \cdot (\vec{A} \times \nabla \theta^m) \end{aligned} \quad (18)$$

The conjugate momenta are

$$\vec{\Pi} = a \mathbb{K} \partial_\eta \vec{\theta} \quad (19)$$

$$\vec{\Pi}^A = \frac{1}{a} \partial_\eta \vec{A} \quad (20)$$

and the Hamiltonian element (spatial density times volume element) is

$$\begin{aligned} \epsilon = & \frac{a}{2} \left( \vec{\Pi}^A \cdot \vec{\Pi}^A + G_{lm} \nabla \theta^l \cdot \nabla \theta^m \right) \\ & + \frac{1}{2a} \left( \vec{\Pi} \mathbb{K}^{-1} \vec{\Pi} + (\nabla \times \vec{A})^2 \right) \\ & + \frac{1}{2a} H_{lm} (\vec{A} \times \nabla \theta^l) \cdot (\vec{A} \times \nabla \theta^m) \end{aligned} \quad (21)$$

The scale factor  $a$  is obtained by integrating the first Friedmann equation,

$$\frac{da}{d\eta} = a \sqrt{\frac{8\pi G_N}{3} \rho_\Sigma a^2 - K} \quad (22)$$

where  $G_N$  is Newton's gravitational constant and  $K$  is the curvature parameter, which can safely be set to 0 (flat space) at least in the early universe. The total energy density  $\rho_\Sigma$  generally has multiple components: a constant vacuum energy density term  $\rho_\Lambda$ , a dust energy density term  $\rho_d \propto 1/a^3$ , a radiation energy density term  $\rho_r \propto 1/a^4$  and a "simulation" energy density term  $\rho$  for the fields on the lattice:

$$\rho_\Sigma = \rho + \rho_\Lambda + \rho_{d0} \left( \frac{a_0}{a} \right)^3 + \rho_{r0} \left( \frac{a_0}{a} \right)^4 \quad (23)$$

The dependence of  $a$  on  $\rho_\Sigma$  breaks the convenient scale invariance of the Minkowski case. To compute it, we need to compute  $\rho$  in physical units:

$$\rho = \frac{\nu^2}{a^3} \epsilon \quad (24)$$

Given a  $\nu$  expressed in  $GeV$ , this yields  $\rho$  in  $GeV^4$ . For more familiar units, apply the conversion factor

$$\begin{aligned} F_\rho &= \frac{\hbar [J \cdot s = kg \cdot m^2/s]}{(c [m/s])(\hbar c [GeV \cdot m])^4} \\ &\simeq 2.320 \cdot 10^{20} \frac{kg}{m^3 \cdot GeV^4} \end{aligned} \quad (25)$$

With  $\nu \simeq 246.3 GeV$ , the physical energy density to use with  $G_N \simeq 6.674 \cdot 10^{-11} m^3/(kg \cdot s^2)$  is

$$F_\rho \rho \simeq \frac{1.407 \cdot 10^{25}}{a^3} \epsilon \frac{kg}{m^3} \quad (26)$$

Compared to the critical density

$$\rho_c = \frac{3}{8\pi G_N} \left( \frac{\dot{a}}{a} \right)^2 \quad (27)$$

for the present-era expansion rate  $H_0 = \dot{a}_0/a_0 \simeq 71 km/s/Mpc \simeq 2.3 \cdot 10^{-18} s^{-1}$ ,

$$\rho_{c0} = \frac{3}{8\pi G_N} H_0^2 \simeq 9.47 \cdot 10^{-27} \frac{kg}{m^3} \quad (28)$$

$F_\rho \rho$  is huge. Requiring

$$F_\rho \rho = \Omega_s \rho_{c0} \quad (29)$$

where  $\Omega_s$  is the fraction of total (= critical) energy density carried by the simulated fields, and solving for  $a$  yields the scale factor

$$a = \nu \sqrt{\frac{\epsilon}{a} \cdot \frac{F_\rho}{\Omega_s \rho_{c0}}} \quad (30)$$

With  $\epsilon/a$  and  $\Omega_s$  both  $\mathcal{O}(1)$ ,  $a \sim 10^{25}$ . To interpret this number, we need the conversion factor from natural time units  $GeV^{-1}$  to seconds:

$$F_t = \frac{\hbar c}{c} \frac{[GeV \cdot m]}{[m/s]} \simeq 6.582 \cdot 10^{-25} GeV \cdot s \quad (31)$$

Since  $\mathcal{L}$  is obtained by dividing out  $\nu^2$  from the effective Lagrangian  $\mathcal{L}_{ETF}$ , Eq. (C18), time and space are scaled up by a factor  $\nu$  on the lattice. A unit lattice time interval therefore translates to a physical time interval  $aF_t/\nu$  seconds, while a unit lattice space step translates to  $c \cdot aF_t/\nu$  meters. With  $a \sim 10^{25}$ , unit lattice time and space steps correspond to  $\mathcal{O}(10^{-2})$  seconds and  $\mathcal{O}(10^6)$  meters, respectively. This is a macroscopic, but far from cosmological scale. For any realistic lattice size and run-time, metric expansion will therefore be completely negligible.

There are two messages here. One is that with this particular choice of parameters, we might as well run the simulation in plain, static Minkowski space. The other is that  $F_\rho \rho \sim \rho_{c0}$  can not be achieved in a way consistent with observation by simply rescaling a realistically sized lattice. Eq. (30) shows that changing  $\nu$  (e.g. by identifying it with the symmetry-breaking scale of a GUT) does not help for  $\epsilon/a$  weakly dependent on  $a$ , as evidenced by Eq. (21): to leading order,  $a$  is then  $\propto \nu$ , so the physical distance  $c(aF_t/\nu)$  corresponding to a unit lattice step is unaffected by such changes. This poses a major obstacle to the simulation of domain boundaries contributing cosmologically significant energy densities.

In principle, it is not hard to simulate such boundaries by tweaking the expressions for  $\rho_\Sigma$  and initial  $a$  to reflect large, empty and therefore ignorable bulk volumes such that average  $\rho_\Sigma \sim \rho_{c0}$ . Suppose we push  $\rho$  all the way up to the neutrino pair production threshold,  $\rho = (10^{-9} GeV)^4$  given a maximally optimistic neutrino mass estimate  $m_\nu = 1 eV$ . Then  $F_\rho \rho \simeq 2.32 \cdot 10^{-16} kg/m^3$ . If this is the energy density of the domain boundaries, equality of average energy density with  $\rho_{c0}$  implies a boundary to bulk volume ratio  $4.08 \cdot 10^{-11}$  (with  $m_\nu = 0.1 eV$ , this reduces to  $4.08 \cdot 10^{-7}$ ). For boundary volume proportional to cell surface, and cell surface proportional to radius squared, this is also roughly the ratio of boundary width to cell radius. In terms of polyhedral cells with edges of length  $r$  and volume  $\propto r^3$ , the boundary volume can be computed by subtracting the volume of cells with edges of length  $r(1-b)$ , where  $b \in [0, 1]$ . The fraction of total volume in boundaries is then  $1 - (1-b)^3$ , and a simulation focusing on the boundaries can be adapted to this scenario by the substitution

$$\rho \rightarrow (1 - (1-b)^3) \rho \quad (32)$$

in the expressions for  $\rho_\Sigma$  and initial  $a$ :

$$\rho_\Sigma = (1 - (1-b)^3) \rho + \rho_\Lambda + \rho_{d0} \left(\frac{a_0}{a}\right)^3 + \rho_{r0} \left(\frac{a_0}{a}\right)^4 \quad (33)$$

$$a = \nu \sqrt{(1 - (1-b)^3) \frac{\epsilon}{a} \cdot \frac{F_\rho}{\Omega_s \rho_{c0}}} \quad (34)$$

The edge length  $r$  is undetermined. Ideally, it should be set by the physics which created the cell structure. Absent that, we can choose a cell size consistent with observation and (ideally at least) run the simulation in reverse, from the present back toward the big bang.

The problem is that  $a$  is now smaller by a factor  $\sqrt{1 - (1-b)^3}$ . For  $m_\nu = 1 eV$ , that's  $\mathcal{O}(10^{-6})$ . The unit lattice time interval is shorter by the same factor, so we are even further away from being able to simulate the evolution of the boundaries on cosmological time scales. The remaining options are to reduce  $\Omega_s$ , i.e. give up on  $F_\rho \rho \sim \rho_{c0}$ , or trying to find an approximately static configuration which allows the use of very long time steps.

By Eq. (30), going down the first route implies making  $a$  larger, which in turn means making the conformal time step  $\Delta_\eta$  smaller. To see this, discretize Eq. (22) and turn it around to find

$$\Delta_\eta = \left(\frac{\Delta_a}{a}\right) \frac{1}{aH} \quad (35)$$

where  $H = \dot{a}/a$  and  $K = 0$  for simplicity. Suppose we want one step on the lattice to be equivalent to 0.1 billion light years, making 64 steps a cosmologically respectable distance of 6.4 billion light years. By Eq. (30), this implies  $a \sim 10^{34}$  which, along with  $H = H_0$ , produces a factor  $aH \sim 10^{16}$  in the denominator of Eq. (35). Since we must also have  $\Delta_a/a \ll 1$  to make the evolution of  $a$  acceptably smooth, it follows that  $\Delta_\eta \ll 10^{-16}$ . With a reasonable choice of  $\Delta_a/a = 10^{-5}$ , the time step going into the integrator becomes  $\Delta_\eta = 10^{-21}$ . This is such a small number that the dynamics of the simulated fields never crosses the threshold into the realm of finite precision computer arithmetics, other than for comparably small initial values. For field values  $\sim 1$ , even the 15 to 17 significant digits of double precision arithmetic simply leave a static initial configuration frozen in place as  $a$  evolves.

Since the problem arises in the product  $aH$ , the choice stands between just making the scale factor  $a$  smaller, again retreating from cosmological scales, or also making the expansion rate  $H$  larger, which implies going back to earlier times.

## B. Three months, five billion years

Faced with the choice of initial conditions on FRW, it is tempting to work in reverse: put a static configuration in a universe with the currently observed properties, then

evolve the equations of motion and the Friedmann equation backwards, toward the bang. The obvious problem with this idea is that random configurations produced by local minimization of static energy density are generally unstable, and therefore extraordinarily unlikely outcomes of random initial conditions. It is one thing to balance a pencil on its tip and watch it fall, quite another to have it end up standing on its tip after being thrown in the air. The latter implies finely tuned initial conditions.

In practice, the reverse approach fails anyway because of limited numerical resolution. For scale factors  $a$  large enough to bring the lattice spacing to cosmological size, the conformal time step  $\Delta_\eta$  is so small that the field configuration remains essentially frozen in place as the universe shrinks, due to numerical truncation.

Forward evolution of smaller volumes works, but as demonstrated by the simulation reported in this section, the computational cost of covering a significant fraction of the history of the universe is substantial.

The initial conditions for this run were chosen to be interesting rather than to conform with any particular cosmological model (a scenario to which this simulation might be directly applicable is a late inflationary event). The same static field configuration consisting of 10 Voronoi cells was used as in the previous examples in Minkowski space (with  $\vec{A} \rightarrow a\vec{A}$  in order not to spoil energy minimization), the expansion rate was set to  $H = 3 \cdot 10^4 \text{ km/s/Mpc}$ , and the fraction of total energy density contributed by the simulated fields was pushed to the smallest power of ten which the integrator could handle,  $\Omega_s = 10^{-35}$ . The rationale for the latter choice is that smaller  $\rho$  implies larger scale factor  $a$ , and we are interested in cosmological scales.

Working back from critical density at the chosen  $H$ ,  $\Omega_s = 10^{-35}$  implies an initial scale factor  $a \simeq 2.1 \cdot 10^{40}$ , which translates to  $1.8 \cdot 10^6$  light years per lattice unit. Energy density was split equally between matter and radiation (negligible contribution from the simulated fields aside). This constitutes a departure from standard cosmology, where matter/radiation equality occurred at redshift  $z \simeq 3200$ , roughly  $57 \cdot 10^3$  years after the bang. In that context, any correlated domains would therefore start out at least a couple of orders of magnitude smaller than a single lattice unit. In other words, the diameter of the initial domains used in this simulation is roughly  $10^3$  times larger than what might be expected in standard cosmology. Temperature might also still be too high at the start of the simulation for  $\mathcal{L}$  to apply unmodified (a convenient line of demarcation is recombination, which occurred at  $z \simeq 1100$  and a temperature  $\simeq 4000 \text{ K} \simeq 0.3 \text{ eV}$ , roughly a factor 3 below matter/radiation equality).

Keep in mind that the scale factor  $a$  affects space and conformal time equally; making it 1000 times smaller would also make time steps 1000 times shorter. Even with the chosen  $a$  and initial  $\Delta_a/a = 10^{-5}$ , 1 191 255 iterations were needed to reach  $a \simeq 6.4 \cdot 10^{41}$ , a roughly 30-fold expansion covering one third of the current age

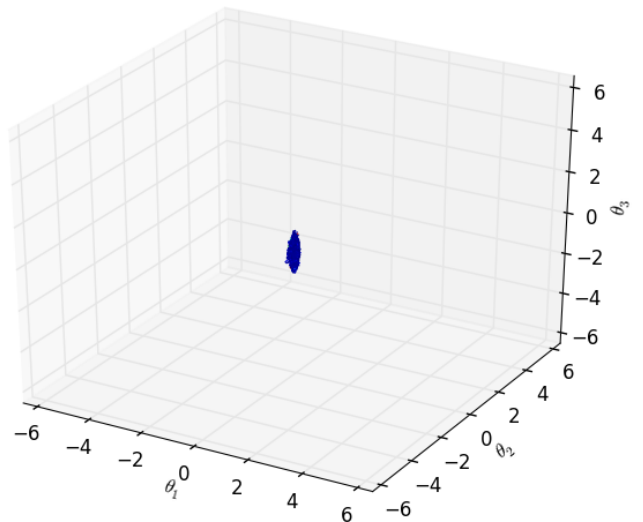


FIG. 40: FRW, scatter plot of  $\vec{\theta}$  at end of run.

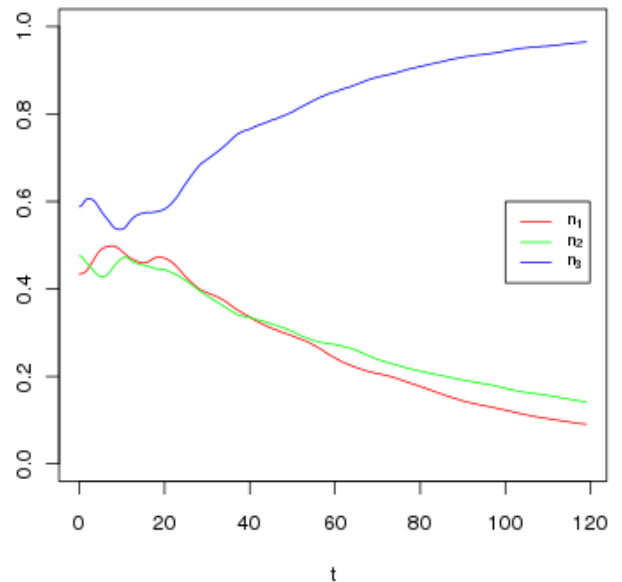


FIG. 41: FRW, evolution of average  $n_a = |\theta_a|/|\vec{\theta}|$ .

of the universe. In wall clock terms, this took almost three months of uninterrupted running (terminated by a blackout), pushing the limit for what can reasonably be done with currently available commodity hardware.

In Figs. 41-44, time is shown as  $\times 10^4$  iterations. The number of iterations is proportional to conformal time, so real time is accelerating; one pixel at the right end of the time axis is worth more than 30 pixels at the left end. As usual,  $\vec{\theta}$  is driven to  $\theta_1 = \theta_2 = 0$ , but there is a notable deviation from previous simulations. After about  $10^5$  iterations, the electric field's contribution to total (field simulation) energy density starts climbing and never looks back (Fig. 44).

To compare with the Minkowski case, we can exploit

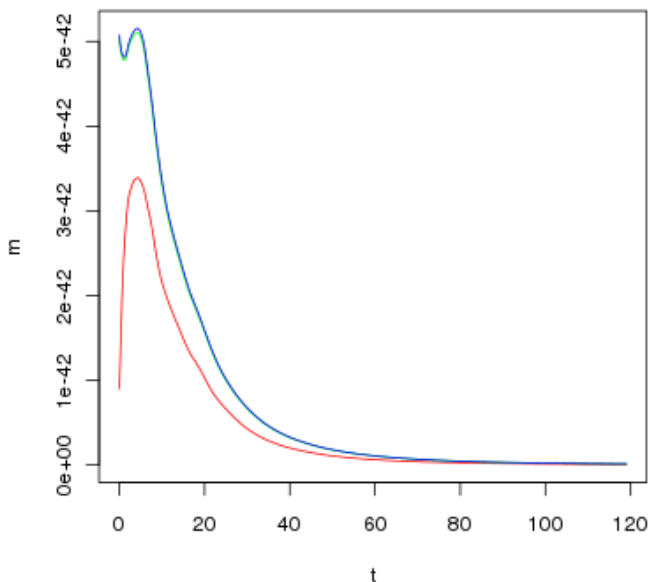


FIG. 42: FRW, evolution of average photon mass eigenvalues.

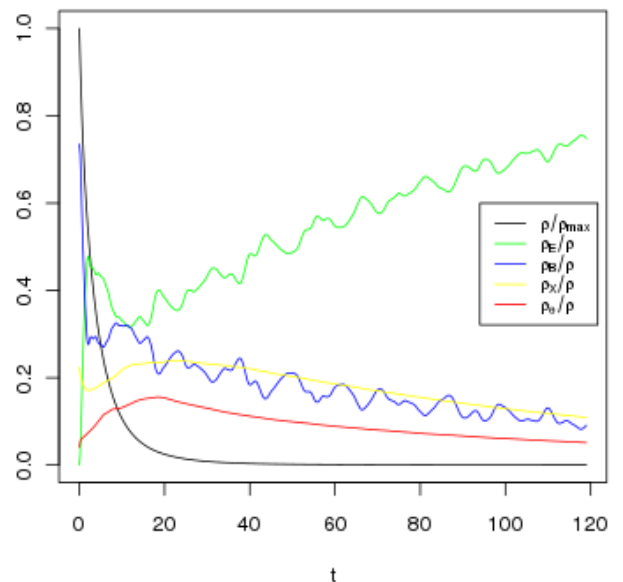


FIG. 44: FRW, evolution of contributions to total energy.

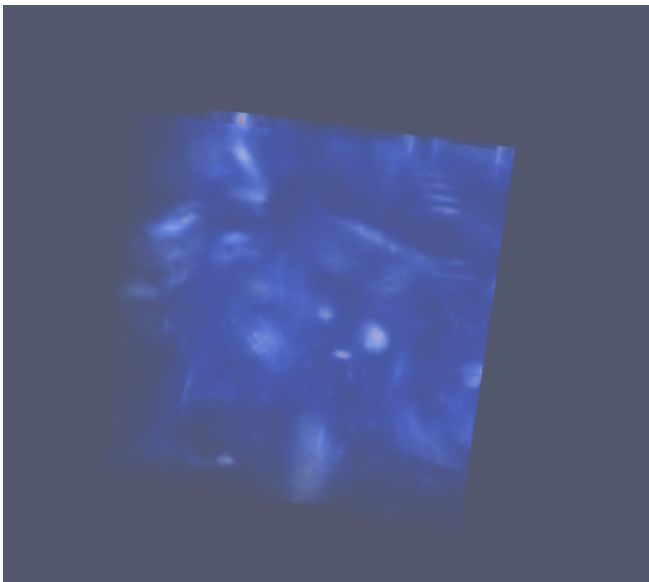


FIG. 43: FRW, energy density at end of run.

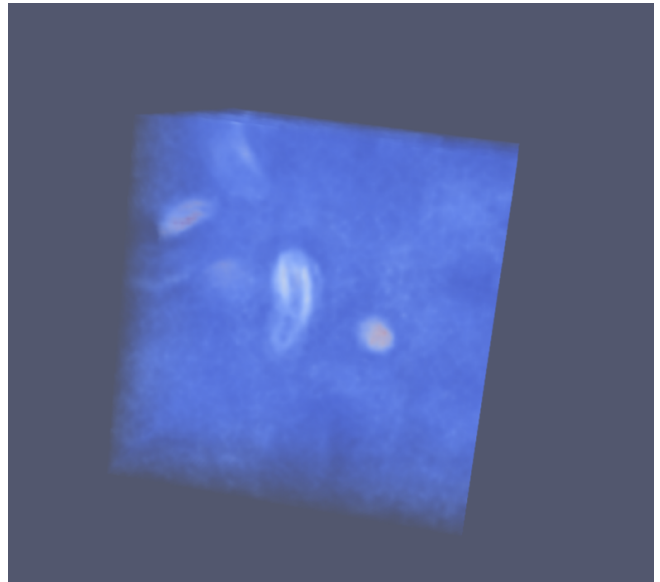


FIG. 45: FRW, high photon mass eigenvalue at end of run.

the scale invariance of the latter to set its  $a$  equal to the starting value for the FRW case. Total simulated time is then  $\propto a$  for Minkowski,  $\propto \int d\eta a(\eta)$  for FRW. At  $10^5$  iterations, the FRW scale factor is  $a \simeq 4.4 \cdot 10^{40}$ , 2.1 times larger than at the start. The integral over  $a(\eta)$  contributes a factor  $\simeq (2.1+1)/2 \simeq 1.5$ , so the equivalent elapsed time in the Minkowski case is at roughly  $1.5 \cdot 10^5$  iterations. The Minkowski simulation then goes on for  $10^5$  more iterations with electric field energy remaining in a steadily declining trend. Evidently, the FRW simulation is doing something qualitatively different.

Physically, the prime suspect is opposite charges be-

ing pulled apart by metric expansion. Superimposed on the overall trend, you can see the same back-and-forth between electric and magnetic field energy as in the Minkowski case, indicating the presence of plasma oscillations. But on an expanding background, such oscillations are biased: maximum separation between charges gets an extra push, pumping up  $\vec{E}$ , while maximum velocity is reduced, damping  $\vec{B}$ .

The difference is clearly discernible in visualizations of energy densities and photon mass eigenvalues. At the end of the simulation, a stable foam-like structure has emerged, consisting of large “bubbles” where pho-

ton mass is low, separated by domain boundaries where photon mass is higher (Figs. 43, 45).

These stable structures emerge about  $1/4$  into the simulation, at  $3 \cdot 10^5$  iterations. The scale factor is then  $a \simeq 1.1 \cdot 10^{41}$ , 5.2 times larger than at the start. The time factor contributed by the sum over  $a(\eta)$  is now  $\simeq (5.2 + 1)/2 \simeq 3.1$ , so the equivalent point in the Minkowski case would be roughly  $9 \cdot 10^5$  iterations, well beyond the end of the actual simulation. Since the growth of the electric field contribution to energy starts much earlier and lacks a counterpart in the Minkowski case, there is no particular reason to expect this kind of stable configurations to emerge there.

There is reason for caution: the integrator is working near the limit of its stable range, and at the end of the simulation,  $\langle \nabla \cdot \vec{E} \rangle \sim -3.7 \cdot 10^{-60}$  while  $\langle q \rangle \sim 1.2 \cdot 10^{-89}$ , so charge conservation seems to be respected significantly better than Gauss' law. It is not inconceivable that we are looking at numerical artifacts caused by the combination of slowing dynamics and growing scale factor,  $a \sim 6.4 \cdot 10^{41}$  at the end of the simulation. But it is certainly encouraging that the plasma oscillation pattern seen in the Minkowski case is reproduced, and that it suggests a physical mechanism for the observed behavior.

Finally, what about the problem which originally motivated the whole effort, light propagation?

The overall mass scale is minuscule. Multiplying the eigenvalues,  $\sim 10^{-44}$  at the end of the simulation, by  $\nu \simeq 246.3 \text{ GeV}$  yields  $\sim 10^{-33} \text{ eV}$ , far below current photon mass bounds. Photon deflection is therefore negligible (see Appendix E). Scale dependence is  $\propto 1/a$ , so even scaling down domain size by a factor 1000 makes no detectable difference (assuming of course that the dynamics remain unchanged under such rescaling).

Unsurprisingly, applying Eq. (1) between each lattice site and its 26 nearest neighbors yields a very different residual luminosity distribution than the simple step function of Appendix B. With  $\vec{\theta}$  closely clustered around  $\vec{\theta} = 0$ , losses between neighbors are in the fourth decimal; see Fig. 46. But they build up over longer distances. Figs. 47 and 48 show the distribution obtained by shooting a million straight rays of length 31.5 (lattice units) in random directions from the center of the simulation cube at the end of the simulation (ignoring light propagation time, not unreasonable given the essentially static configuration) and updating their residual luminosity when they cross into new cells (defined as the Voronoi cells of lattice sites). Average luminosity loss is now roughly 3%. The corresponding physical distance is  $1.7 \cdot 10^9$  light years.

Keep in mind that this simulation uses initial conditions which are questionable at best (domains start out 1000 times larger than we have a right to expect) and ends at only one third of the current age of the universe. The implicit assumption that Eq. (1) remains valid in the absence of clearly defined domains may also be overly simplified.

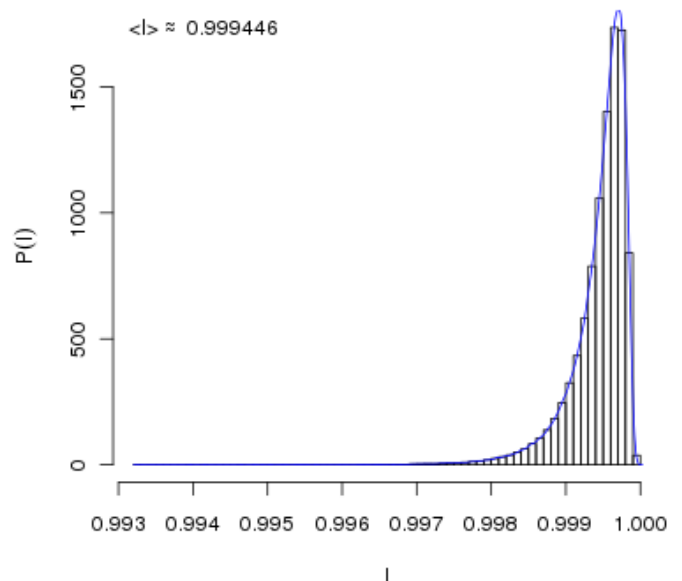


FIG. 46: FRW, nearest neighbor residual luminosity distribution at end of run.

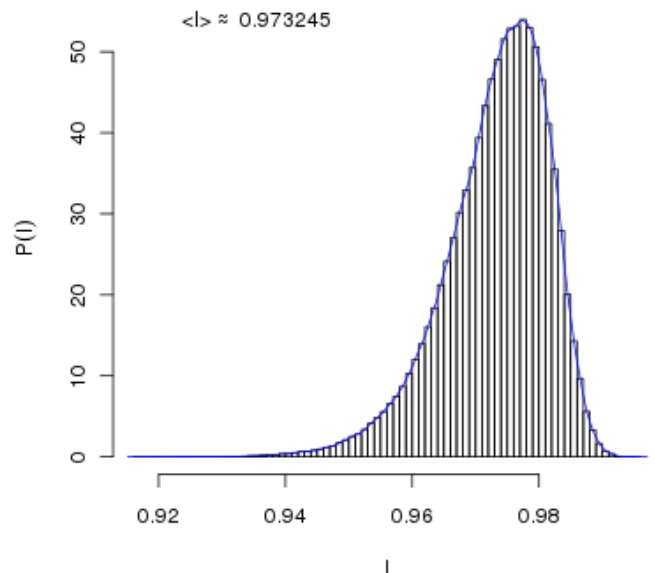


FIG. 47: FRW, residual luminosity distribution on (or from) sphere with radius 31.5 (lattice units) at end of run.



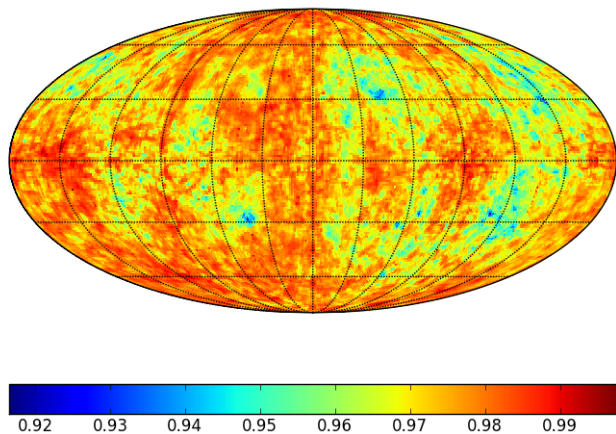


FIG. 48: FRW, residual luminosity on (or from) sphere with radius 31.5 (lattice units) at end of run, Mollweide projection.

## VI. DISCUSSION

Every simulation I have run to date supports the conclusion that the line  $\theta_1 = \theta_2 = 0$  is an attractor of  $\mathcal{L}$ , growing in strength with electromagnetic energy density. The larger the latter, the more  $\vec{\theta}$  spreads out along the  $\theta_3$  axis, giving its scatter plot a cigar-like shape.

Since even the simplest case takes a week to run, the number of simulations I have been able to carry out is limited, and it would certainly be desirable to explore the behavior of  $\mathcal{L}$  in greater detail. But once noticed, the special nature of  $\theta_1 = \theta_2 = 0$  is evident by inspection, and its physical origin is clear. The inclusion of more physics (self-gravity, interactions with QCD condensates) may modify this picture, but let us start by considering what it implies on its own.

In Minkowski space, and therefore on scales where metric expansion is negligible, the basic lesson seems to be that when electromagnetic energy density is comparable to the energy density of a disordered  $\vec{\theta}$  configuration, as might reasonably be expected from equipartition,  $\vec{\theta}$  will generally settle around  $\theta_1 = \theta_2 = 0$  in the time needed for a few collisions between wavefronts, so essentially on a time scale comparable to the  $\vec{\theta}$  configuration's characteristic wavelength. On the other hand, the simulations suggest that photon mass never falls all the way to zero. Rather, as the coupling between  $\vec{A}$  and  $\vec{\theta}$  becomes smaller, the radiation pressure towards  $\theta_1 = \theta_2 = 0$  is eventually balanced by the thermal motion of  $\vec{\theta}$ , and the “cigar” distribution in  $\vec{\theta}$  space stabilizes. Deviations from  $\theta_1 = \theta_2 = 0$  may never become so small that they have negligible effects on photon propagation over cosmological distances.

On the FRW metric, the simulation reported here suggests that the rapid expansion of the early universe may have aided charge separation and the formation of long-lived structures. Serious hardware resources would be

needed to explore this possibility properly. In this context, it is worth noting that neutral domains with electrically charged boundaries have been proposed in the past [56][57] as sites of baryogenesis [58], as dark matter candidates [59] and even as an explanation for dark energy [60].

$\vec{\theta}$  configurations stabilized by magnetic fields are also conceivable (see Eq. (D21)) and may have important consequences. A notable example is the suggestion that primordial magnetic fields seeded by long-lived electroweak strings caused an alignment of quasar axes on cosmological scales [61]. More generally, the suspicious alignment between the polarization of quasar light and CMB low multipole moments [62] may be trying to tell us something.

It should be kept in mind that any constant  $\vec{\theta}$  decouples from  $\vec{A}$ . If electroweak symmetry breaking combined with a mildly inflationary event to create a number of domains within the observable universe, each filled with effectively constant  $\vec{\theta}$  in the bulk, the regions primarily subject to pressure toward  $\theta_1 = \theta_2 = 0$  would be the domain boundaries, where  $\vec{\theta}$  interpolates between adjacent domains. The realignment would be fast where  $\vec{\theta}$  varies rapidly, slow where it varies slowly, so it would spread from the centers of the boundaries, eating into the domains. How fast would this process be? I don't know. All I know is that it must be subluminal. So if Higgs-scale inflation produced domains smaller than the current Hubble volume, they might contribute to the luminosity deficit of distant SNe Ia.

But suppose that the drive towards  $\theta_1 = \theta_2 = 0$  is very efficient, so that for all practical purposes,  $\theta_3$  really is the only remaining degree of freedom.  $\mathcal{L}$  then reduces to plain Klein-Gordon (plus decoupled electromagnetism). It would still be unwise to ignore this invisible  $\theta_3$ . To start with, it (presumably) gravitates. If we want it to carry a significant fraction of the energy density of the universe, there is no reason to expect its self-gravity to be less important than that of ordinary matter. The simplest case one might envision are the gravitating, infinite, plane NLSM domain boundaries studied analytically by van Holten [63]–[66]. These turn out to be essentially unaltered plane wave solutions of the field equations in Minkowski space, traveling at the speed of light and accompanied by pp-type gravitational waves. The effect of the latter on test particles is to induce oscillations in the plane orthogonal to the direction of propagation and linear motion plus oscillations along the direction of propagation.

As usual, once domain size is made finite and boundaries start interacting with each other, the problem becomes analytically intractable and one must turn to numerical methods. This is not something which seems possible to tackle meaningfully with current (spring 2012) commodity hardware.

QCD condensates may also alter the picture. It is a straightforward exercise to substitute expectation val-

ues for quark bilinears  $\langle \bar{q}q \rangle$  into the Standard Model Lagrangian's quark mass terms and verify that they do not affect  $\theta_1$  and  $\theta_2$ , assuming absence of charged quark condensates. Not so for  $\theta_3$ . A conceivable consequence of QCD's chiral phase transition could therefore be to lock the value of  $\theta_3$ , squeezing the cigar shape of the  $\vec{\theta}$  distribution into a disk. And that could help explain not only why we see something rather than nothing, but even why there is something to see at all [67].

## APPENDIX A: RESIDUAL LUMINOSITY

This is the original derivation of the residual luminosity  $\ell(\vec{\omega})$  from [38], modulo typographic polish. See Appendix C for a more intuitive alternative.

In the standard  $SU(2) \times U(1)$  model of electroweak interactions [68][69][70], the  $U(1)$  gauge field  $B_\mu$  and the three  $SU(2)$  gauge fields  $W_\mu^j$  are collected in the matrix (the field-dependent part of the covariant derivative)

$$\mathbb{W}_\mu = \begin{bmatrix} g_B B_\mu + g_W W_\mu^3 & g_W W_\mu^1 - i g_W W_\mu^2 \\ g_W W_\mu^1 + i g_W W_\mu^2 & g_B B_\mu - g_W W_\mu^3 \end{bmatrix} \quad (A1)$$

( $g_W = SU(2)$  coupling constant;  $g_B = U(1)$  coupling constant) acting on weak isospin doublets. Given an arbitrary  $\mathbb{W}_\mu$ , we can decompose it into individual gauge fields using

$$B_\mu = \frac{1}{2g_B} \text{Tr} [\tau_0 \mathbb{W}_\mu] \quad (A2)$$

$$W_\mu^1 = \frac{1}{2g_W} \text{Tr} [\tau_1 \mathbb{W}_\mu] \quad (A3)$$

$$W_\mu^2 = \frac{i}{2g_W} \text{Tr} [\tau_2 \mathbb{W}_\mu] \quad (A4)$$

$$W_\mu^3 = \frac{1}{2g_W} \text{Tr} [\tau_3 \mathbb{W}_\mu] \quad (A5)$$

where all traces are understood to be over weak isospin space only,  $\tau_0 = \mathbf{1}_2$  and  $\tau_1, \tau_2, \tau_3$  are the Pauli matrices

$$\tau_1 = \begin{bmatrix} 0 & 1 \\ 1 & 0 \end{bmatrix} \quad \tau_2 = \begin{bmatrix} 0 & -i \\ i & 0 \end{bmatrix} \quad \tau_3 = \begin{bmatrix} 1 & 0 \\ 0 & -1 \end{bmatrix} \quad (A6)$$

The photon  $A_\mu$  and the neutral weak vector boson  $Z_\mu^0$  are defined as the linear combinations

$$\begin{bmatrix} Z_\mu^0 \\ A_\mu \end{bmatrix} = \begin{bmatrix} \cos(\theta_W) & -\sin(\theta_W) \\ \sin(\theta_W) & \cos(\theta_W) \end{bmatrix} \begin{bmatrix} W_\mu^3 \\ B_\mu \end{bmatrix} \quad (A7)$$

where  $\theta_W$  is the Weinberg (weak mixing) angle,

$$g_W \sin(\theta_W) = g_B \cos(\theta_W) = e > 0 \quad (A8)$$

( $e$  = electric charge of the proton). Combining Eqs. (A2), (A5) and (A7), we can therefore write

$$A_\mu = \frac{\sin(\theta_W)}{2g_W} \text{Tr} [\tau_3 \mathbb{W}_\mu] + \frac{\cos(\theta_W)}{2g_B} \text{Tr} [\tau_0 \mathbb{W}_\mu] \quad (A9)$$

Setting  $Z_\mu^0 = W_\mu^1 = W_\mu^2 = 0$  and  $A_\mu = 1$ , inverting Eq. (A7) and plugging the results into Eq. (A1) yields  $\mathbb{W}_\mu$  for a normalized pure photon state:

$$\mathbb{W}_\mu^A = \begin{bmatrix} 2e & 0 \\ 0 & 0 \end{bmatrix} \quad (A10)$$

Now consider the effect on  $\mathbb{W}_\mu$  of a global  $SU(2) \times U(1)$  transformation

$$\mathbb{U} = \exp \left( \frac{i}{2} \omega_0 \tau_0 + \frac{i}{2} \omega_j \tau_j \right) \quad (A11)$$

with  $U(1)$  parameter  $\omega_0$  and  $SU(2)$  parameters  $\vec{\omega} = [\omega_1, \omega_2, \omega_3]$ :

$$\mathbb{W}_\mu \rightarrow \mathbb{W}'_\mu = \mathbb{U} \mathbb{W}_\mu \mathbb{U}^\dagger \quad (A12)$$

Substituting this into Eq. (A9) and using the cyclic property of the trace,

$$A_\mu \rightarrow A'_\mu = \frac{\sin(\theta_W)}{2g_W} \text{Tr} [\mathbb{U}^\dagger \tau_3 \mathbb{U} \mathbb{W}_\mu] + \frac{\cos(\theta_W)}{2g_B} \text{Tr} [\mathbb{W}_\mu] \quad (A13)$$

$U(1)$  transformations associated with  $\omega_0 \tau_0$  drop out. Specializing to the pure photon state  $\mathbb{W}_\mu^A$  of Eq. (A10), introducing the shorthand

$$\omega_\perp^2 = \omega_1^2 + \omega_2^2 \quad (A14)$$

$$\omega = \sqrt{\omega_\perp^2 + \omega_3^2} \quad (A15)$$

and doing the traces, Eq. (A13) reduces to

$$A_\mu \rightarrow A'_\mu = \ell(\vec{\omega}) A_\mu \quad (A16)$$

with

$$\ell(\vec{\omega}) = \sin^2(\theta_W) \frac{\omega_\perp^2 \cos(\omega) + \omega_3^2}{\omega^2} + \cos^2(\theta_W) \quad (A17)$$

Together with Eq. (A16), Eq. (A17) describes the effect of a global transformation with  $SU(2)$  parameters  $\vec{\omega}$  (and arbitrary  $U(1)$  parameter  $\omega_0$ ) on a pure photon state. On its own, since  $A_\mu$  is proportional to the photon number operator, it gives us the fraction of photons surviving the transformation.

## APPENDIX B: RESIDUAL LUMINOSITY DISTRIBUTIONS

This is the derivation of the PDF for residual luminosity from [38], as amended in November 2008.

The vacuum manifold of  $\Phi$  is a 3-sphere. The  $SU(2)$  parameters  $\vec{\omega}$  of Eq. (1) can be mapped to Cartesian coordinates of an embedding 4-dimensional Euclidean space ( $\mathbb{R}^4$ ) by

$$\omega/2 = \arccos(n_0) \quad (B1)$$

$$\vec{\omega} = \frac{\omega \vec{n}}{\sin(\omega/2)} \quad (B2)$$

so that

$$(n_0)^2 + (n_1)^2 + (n_2)^2 + (n_3)^2 = 1 \quad (\text{B3})$$

Substituting Eqs. (B1)-(B2) into Eq. (1) yields

$$\ell(\vec{n}) = 1 - 2n_\perp^2 \sin^2(\theta_W) \quad (\text{B4})$$

i.e. luminosity is determined by

$$n_\perp^2 = n_1^2 + n_2^2 \quad (\text{B5})$$

The PDF for residual luminosity therefore follows from that of  $n_\perp^2$  over the unit 3-sphere. For uniformly distributed  $\vec{n}$ , it is simply a step function,  $P_1(\ell) > 0$  for  $\ell \in [1 - 2\sin^2(\theta_W), 1]$ .

Given  $P_1(\ell)$ , the distribution of the residual luminosity  $\ell = \ell_1 \cdot \ell_2 \cdot \dots \cdot \ell_n$  after  $n$  crossings between  $n+1$  domains with independent  $\langle \Phi \rangle$  can be obtained using Rohatgi's result for the distribution of the product of two stochastic variables [71]:

$$P_2(\ell = \ell_1 \cdot \ell_2) = \int_\ell^1 dx P_1(x) P_1(\ell/x)/x \quad (\text{B6})$$

and generally

$$P_{n+1}(\ell = \ell_1 \cdot \ell_2 \cdot \dots \cdot \ell_n) = \int_\ell^1 dx P_1(x) P_n(\ell/x)/x \quad (\text{B7})$$

### APPENDIX C: EFFECTIVE LAGRANGIAN

This is the derivation of the low energy effective Lagrangian of electroweak interactions ( $\mathcal{L}_{EFT}$ ) from [72].

The shortest route to  $\mathcal{L}_{EFT}$  starts with the gauged non-linear sigma model (GNLSM), valid for energies  $\ll$  the Higgs mass, which was written down long ago to parametrize the unknown symmetry breaking sector [73][74][75] (see Ch. 2 in [76] for a review). It amounts to constraining the Higgs field  $\Phi$  to the vacuum manifold (the 3-sphere with radius  $\nu$ ) by collecting its components in the SU(2) matrix

$$\begin{bmatrix} \phi^{0\dagger} & \phi^+ \\ -\phi^{+\dagger} & \phi^0 \end{bmatrix} = \frac{\nu}{\sqrt{2}} \Sigma \quad (\text{C1})$$

with

$$\Sigma = e^{i\theta_a \tau_a/2} = \cos(\theta/2) + i \frac{\theta_a \tau_a}{\theta} \sin(\theta/2) \quad (\text{C2})$$

$$\theta = \sqrt{(\theta_1)^2 + (\theta_2)^2 + (\theta_3)^2} \quad (\text{C3})$$

The covariant derivative acting on  $\Sigma$  is

$$\mathbb{D}_\mu = \partial_\mu + i \frac{g_W}{2} W_\mu^a \tau^a - i \frac{g_B}{2} B_\mu \tau^3 \quad (\text{C4})$$

and the full Lagrangian is

$$\begin{aligned} \mathcal{L}_{GNLSM} = & -\frac{1}{4} B_{\mu\nu} B^{\mu\nu} - \frac{1}{4} W_{\mu\nu}^a W^{a\mu\nu} \\ & + \frac{\nu^2}{4} \text{Tr} \left[ (\mathbb{D}_\mu \Sigma)^\dagger (\mathbb{D}^\mu \Sigma) \right] \end{aligned} \quad (\text{C5})$$

It has been used as is to compute the one-loop thermal effective action for an electroweak plasma at temperatures below the mass of a (heavy) Higgs and above that of the weak gauge bosons [77], but we are interested in the real low energy limit, where the massive gauge bosons can not be excited either and must be set to zero along with radial Higgs excitations. We therefore need to isolate the linear combination of gauge fields with vanishing mass, i.e. the photon, as defined in an arbitrary vacuum  $\vec{\theta} = [\theta_1, \theta_2, \theta_3]$ .

In the basis  $[B_\mu, W_\mu^1, W_\mu^2, W_\mu^3]$ , the  $\mathcal{L}_{GNLSM}$  terms quadratic in  $B_\mu$  and  $W_\mu^a$  give rise to the mass matrix

$$\frac{\nu^2}{2} \begin{bmatrix} g_B^2 & g_B g_W \Theta_1 & g_B g_W \Theta_2 & -g_B g_W \Theta_3 \\ g_B g_W \Theta_1 & g_W^2 & 0 & 0 \\ g_B g_W \Theta_2 & 0 & g_W^2 & 0 \\ -g_B g_W \Theta_3 & 0 & 0 & g_W^2 \end{bmatrix} \quad (\text{C6})$$

where we have introduced the convenient auxiliary quantities

$$\Theta_1 = [\theta_1 \theta_3 (\cos(\theta) - 1) + \theta \theta_2 \sin(\theta)] / \theta^2 \quad (\text{C7})$$

$$\Theta_2 = [\theta_2 \theta_3 (\cos(\theta) - 1) - \theta \theta_1 \sin(\theta)] / \theta^2 \quad (\text{C8})$$

$$\Theta_3 = [(\theta_1^2 + \theta_2^2) \cos(\theta) + \theta_3^2] / \theta^2 \quad (\text{C9})$$

satisfying  $(\Theta_1)^2 + (\Theta_2)^2 + (\Theta_3)^2 = 1$ . The eigenvalues of Eq. (C6) are the tree level masses squared of photon,  $W^\pm$  and  $Z^0$ . The two degenerate eigenstates can be orthogonalized to obtain

$$\mathcal{A}_\mu \propto [g_W/g_B, -\Theta_1, -\Theta_2, \Theta_3] \quad (\text{C10})$$

$$\hat{W}_\mu^1 \propto [0, -\Theta_2, \Theta_1, 0] \quad (\text{C11})$$

$$\hat{W}_\mu^2 \propto [0, \Theta_1 \Theta_3, \Theta_2 \Theta_3, \Theta_1^2 + \Theta_2^2] \quad (\text{C12})$$

$$Z_\mu \propto [-g_B/g_W, -\Theta_1, -\Theta_2, \Theta_3] \quad (\text{C13})$$

Note in passing that normalizing Eq. (C10) and computing its scalar product for  $\vec{\theta} = 0$  and  $\vec{\theta} = \vec{\omega}$  reproduces Eq. (A17), confirming its interpretation as the projection of the photon eigenstate in one vacuum onto the photon eigenstate on another vacuum.

To eliminate the massive bosons, normalize Eqs. (C10)-(C13), invert them, and set  $\hat{W}_\mu^1 = \hat{W}_\mu^2 = Z_\mu = 0$ . The result is

$$B_\mu = \mathcal{A}_\mu \cos(\theta_W) \quad (\text{C14})$$

$$W_\mu^1 = -\mathcal{A}_\mu \Theta_1 \sin(\theta_W) \quad (\text{C15})$$

$$W_\mu^2 = -\mathcal{A}_\mu \Theta_2 \sin(\theta_W) \quad (\text{C16})$$

$$W_\mu^3 = \mathcal{A}_\mu \Theta_3 \sin(\theta_W) \quad (\text{C17})$$

To obtain the low energy EFT of the electroweak boson sector to leading order, substitute Eqs. (C14)-(C17) into

$\mathcal{L}_{GNLSM}$  and find

$$\begin{aligned}\mathcal{L}_{EFT} = & \frac{\nu^2}{8} \left[ \partial_\mu \theta \partial^\mu \theta + \frac{4 \sin^2(\theta/2)}{\theta^2} \left( \frac{\vec{\theta}}{\theta} \times \partial_\mu \vec{\theta} \right)^2 \right] \\ & - \frac{1}{4} (\partial_\mu \mathcal{A}_\nu - \partial_\nu \mathcal{A}_\mu)^2 \\ & - \frac{\sin^2(\theta_W)}{4} (\mathcal{A}_\mu \partial_\nu \Theta_a - \mathcal{A}_\nu \partial_\mu \Theta_a)^2\end{aligned}\quad (C18)$$

The first row in Eq. (C18) is just the plain  $O(4)$  NLSM in polar field coordinates, the second row is the Maxwell Lagrangian, the third row couples them  $\propto \sin^2(\theta_W)$ , acting as an effective photon mass term when  $\vec{\theta}$  is not constant. For any constant  $\vec{\theta}$ ,  $\mathcal{L}_{EFT}$  reduces to plain electromagnetism, as it must.

Specializing to the time-axial gauge,  $\mathcal{A}_0 = 0$ , the electric and magnetic fields are

$$\vec{\mathcal{E}} = -\partial_0 \vec{\mathcal{A}} \quad (C19)$$

$$\vec{\mathcal{B}} = \nabla \times \vec{\mathcal{A}} \quad (C20)$$

Varying  $\mathcal{L}_{EFT}$  in  $\mathcal{A}_0$  yields the Gauss constraint

$$\nabla \cdot \vec{\mathcal{E}} = \partial_0 \vec{\theta}^T \mathbb{H} \vec{\mathcal{A}} \cdot \nabla \vec{\theta} \quad (C21)$$

(a plane in  $\vec{\mathcal{A}}$  space) where the matrix  $\mathbb{H}$  has components

$$H_{ab} = \sin^2(\theta_W) \frac{\partial \Theta_c}{\partial \theta_a} \frac{\partial \Theta_c}{\partial \theta_b} \quad (C22)$$

and no negative eigenvalues.

This completely fixes the gauge, leaving  $\vec{\mathcal{A}}$  with only two independent degrees of freedom. Energy density can now be written as a sum of quadratic forms,

$$\begin{aligned}\rho = & \frac{1}{2} (\vec{\mathcal{E}}^2 + \vec{\mathcal{B}}^2) \\ & + \frac{1}{2} \partial_0 \vec{\theta}^T (\nu^2 \mathbb{G} + \vec{\mathcal{A}}^2 \mathbb{H}) \partial_0 \vec{\theta} \\ & + \frac{\nu^2}{2} \partial_m \vec{\theta}^T \mathbb{G} \partial_m \vec{\theta} \\ & + \frac{1}{2} (\varepsilon_{jkl} \mathcal{A}_k \partial_l \vec{\theta})^T \mathbb{H} (\varepsilon_{jmn} \mathcal{A}_m \partial_n \vec{\theta})\end{aligned}\quad (C23)$$

where  $\mathbb{G}$ , with components

$$G_{ab} = \left( \frac{\delta_{ad} \delta_{be}}{2} + \frac{1 - \cos \theta}{\theta^2} \varepsilon_{cda} \varepsilon_{ceb} \right) \frac{\theta_d \theta_e}{\theta^2} \quad (C24)$$

is the 3-sphere metric, with eigenvalues  $1/4$  and (doubly degenerate)  $0 \leq (1 - \cos(\theta))/(2\theta^2) \leq 1/4$ . Since neither  $\mathbb{H}$  nor  $\mathbb{G}$  have negative eigenvalues,  $\rho \geq 0$ .

For numerics, it's convenient to perform the substitution

$$\mathcal{A}_\mu = \nu A_\mu \quad (C25)$$

in  $\mathcal{L}_{EFT}$  and divide out the overall  $\nu^2$  factor. Using Eqs. (C22) and (C24) along with

$$(\partial_\mu A_\nu - \partial_\nu A_\mu)^2 = 2 \partial_\mu A_\nu (\partial^\mu A^\nu - \partial^\nu A^\mu) \quad (C26)$$

and

$$\begin{aligned}(A_\mu \partial_\nu \theta^a - A_\nu \partial_\mu \theta^a)(A^\mu \partial^\nu \theta^b - A^\nu \partial^\mu \theta^b) \\ = 2 A_\mu \partial_\nu \theta^a (A^\mu \partial^\nu \theta^b - A^\nu \partial^\mu \theta^b)\end{aligned}\quad (C27)$$

yields the manifestly scale-free (and by Polyakov's theorem [78] therefore also conformally invariant)

$$\begin{aligned}\mathcal{L} = & \frac{1}{2} G_{ab} \partial_\mu \theta^a \partial^\mu \theta^b \\ & + \frac{1}{2} \partial_\mu A_\nu (\partial^\nu A^\mu - \partial^\mu A^\nu) \\ & + \frac{1}{2} H_{ab} A_\mu \partial_\nu \theta^a (A^\nu \partial^\mu \theta^b - A^\mu \partial^\nu \theta^b)\end{aligned}\quad (C28)$$

## APPENDIX D: STRESS-ENERGY TENSOR

Since we will eventually want to couple  $\mathcal{L}$  to gravity, it's convenient to use the Hilbert stress-energy tensor

$$T^{\mu\nu} = \frac{-2}{\sqrt{-g}} \frac{\delta(\mathcal{L}\sqrt{-g})}{\delta g_{\mu\nu}} \quad (D1)$$

where

$$g = \det g_{\mu\nu} \quad (D2)$$

is the determinant of the metric  $g_{\mu\nu}$  with signature  $+-$  and volume factor  $\sqrt{-g}$ .

$T^{\mu\nu}$  describes the variation of  $\mathcal{L}$  with respect to the metric. When  $\mathcal{L}$  only couples to  $g_{\mu\nu}$  and not to its derivatives (the standard case) the variation is an ordinary derivative, and we can write

$$\begin{aligned}T^{\mu\nu} = & \frac{-2}{\sqrt{-g}} \left( \frac{\partial \mathcal{L}}{\partial g_{\mu\nu}} \sqrt{-g} + \mathcal{L} \frac{\partial \sqrt{-g}}{\partial g_{\mu\nu}} \right) \\ = & -2 \left( \frac{\partial \mathcal{L}}{\partial g_{\mu\nu}} + \frac{\mathcal{L}}{\sqrt{-g}} \frac{\partial \sqrt{-g}}{\partial g_{\mu\nu}} \right)\end{aligned}\quad (D3)$$

By Jacobi's formula for the derivative of a determinant,

$$\begin{aligned}\frac{\partial \sqrt{-g}}{\partial g_{\mu\nu}} &= \frac{g g^{\nu\mu}}{2 \sqrt{-g}} \\ &= \frac{\sqrt{-g}}{2} g^{\mu\nu}\end{aligned}\quad (D4)$$

where  $g^{\nu\mu}$  (the contravariant metric) is the inverse of  $g_{\nu\mu}$  and the metric's symmetry property ( $g_{\nu\mu} = g_{\mu\nu}$ ) is used in the last line. Thus,

$$T^{\mu\nu} = -2 \frac{\partial \mathcal{L}}{\partial g_{\mu\nu}} - \mathcal{L} g^{\mu\nu} \quad (D5)$$

Coupling  $\mathcal{L}$  to gravity amounts to inserting the metric wherever Lorentz indices are contracted and replacing ordinary derivatives with generally covariant ones. The result is on the general form

$$\mathcal{L} = S + g^{\mu\nu} X_{\mu\nu} + g^{\mu\nu} g^{\lambda\rho} Y_{\mu\nu\lambda\rho} + \dots \quad (D6)$$

where  $S$  only depends on scalar quantities (typically scalar potential terms). To compute  $T^{\mu\nu}$  we need to know that

$$\begin{aligned}\frac{\partial g^{\lambda\rho}}{\partial g_{\mu\nu}} &= -g^{\lambda\alpha} \frac{\partial g_{\alpha\beta}}{\partial g_{\mu\nu}} g^{\beta\rho} \\ &= -g^{\lambda\alpha} \delta_{\alpha}^{\mu} \delta_{\beta}^{\nu} g^{\beta\rho} \\ &= -g^{\lambda\mu} g^{\nu\rho}\end{aligned}\quad (\text{D7})$$

where the first line uses the standard expression for the derivative of the inverse of a matrix.

Given  $g^{\mu\nu}$  and  $\mathcal{L}$ , it is now a straightforward algebra exercise to find  $T^{\mu\nu}$ . For any  $g^{\mu\nu}$ ,

$$\begin{aligned}T^{\mu\nu} &= -S g^{\mu\nu} \\ &\quad + (2g^{\lambda\mu} g^{\rho\nu} - g^{\mu\nu} g^{\lambda\rho}) X_{\lambda\rho} \\ &\quad + (2g^{\sigma\mu} g^{\tau\nu} g^{\lambda\rho} + 2g^{\sigma\tau} g^{\lambda\mu} g^{\rho\nu} \\ &\quad - g^{\mu\nu} g^{\sigma\tau} g^{\lambda\rho}) Y_{\sigma\tau\lambda\rho}\end{aligned}\quad (\text{D8})$$

In practice one usually ends up on the FRW metric with time-dependent universal scale factor  $a(t)$ ,

$$g_{\mu\nu} = \text{diag}(1, -a^2(t), -a^2(t), -a^2(t)) \quad (\text{D9})$$

inverse

$$g^{\mu\nu} = \text{diag}(1, -1/a^2(t), -1/a^2(t), -1/a^2(t)) \quad (\text{D10})$$

determinant  $g = -a^6(t)$  and volume factor  $\sqrt{-g} = a^3(t)$ . The only non-vanishing Christoffel symbols are then  $\Gamma_{0j}^i = \delta_j^i \dot{a}(t)/a(t)$ , so only time derivatives are affected. Minkowski space is recovered as the special case  $a = 1$ .

Two quantities of particular interest are the energy density

$$\rho = T^{00} \quad (\text{D11})$$

and pressure

$$p = \frac{-1}{3} T_m^m = \frac{a^2}{3} T^{mm} \quad (\text{D12})$$

Comparing the  $\mathcal{L}$  of Eq. (C28) with Eq. (D6), it's straightforward to read off

$$X_{\mu\nu} = \frac{1}{2} G_{ab} \partial_\mu \theta^a \partial_\nu \theta^b \quad (\text{D13})$$

and

$$\begin{aligned}Y_{\mu\nu\lambda\rho} &= \frac{1}{2} \partial_\mu A_\lambda (\partial^\rho A^\nu - \partial^\nu A^\rho) \\ &\quad + \frac{1}{2} H_{ab} A_\mu \partial_\rho \theta^a (A^\lambda \partial^\nu \theta^b - A^\nu \partial^\lambda \theta^b)\end{aligned}\quad (\text{D14})$$

The only terms involving time derivatives of a Lorentz vector, and therefore the only ones which might conceivably be modified by non-vanishing Christoffel symbols on the FRW metric, are from the Maxwell Lagrangian. But

generally covariant curl equals ordinary curl, so there are in fact no contributions from the Christoffel symbols.

Substituting Eqs. (D13)-(D14) into Eq. (D8), imposing the time-axial gauge  $A_0 = 0$  and applying Eqs. (D11)-(D12) yields

$$\begin{aligned}\rho &= \frac{1}{2} G_{ab} \left( \dot{\theta}^a \dot{\theta}^b + \frac{1}{a^2} \nabla \theta^a \cdot \nabla \theta^b \right) \\ &\quad + \frac{1}{2a^2} \left( \vec{E}^2 + H_{ab} \vec{A}^2 \dot{\theta}^a \dot{\theta}^b \right) \\ &\quad + \frac{1}{2a^4} \left( \vec{B}^2 + H_{ab} (\vec{A} \times \nabla \theta^a) \cdot (\vec{A} \times \nabla \theta^b) \right)\end{aligned}\quad (\text{D15})$$

and

$$\begin{aligned}p &= \frac{1}{2} G_{ab} \left( \dot{\theta}^a \dot{\theta}^b - \frac{1}{3a^2} \nabla \theta^a \cdot \nabla \theta^b \right) \\ &\quad + \frac{1}{6a^2} \left( \vec{E}^2 + H_{ab} \vec{A}^2 \dot{\theta}^a \dot{\theta}^b \right) \\ &\quad + \frac{1}{6a^4} \left( \vec{B}^2 + H_{ab} (\vec{A} \times \nabla \theta^a) \cdot (\vec{A} \times \nabla \theta^b) \right)\end{aligned}\quad (\text{D16})$$

where

$$\vec{E} = -\dot{\vec{A}} \quad (\text{D17})$$

$$\vec{B} = \nabla \times \vec{A} \quad (\text{D18})$$

are the electric and magnetic field, respectively.

Note the negative contribution to pressure from the spatial derivative terms for  $\vec{\theta}$ . By inspection, they are capped at  $-1/3$  of energy density, enough to drive linear, but not accelerated, expansion.

Also worthy of note is the combination of terms  $\propto 1/a^2$  and  $\propto 1/a^4$  in Eq. (D15), which implies that Derrick's theorem [79] does not apply, i.e. static, finite energy solutions (e.g. vortices) can not be ruled out without a detailed analysis. The stability condition (the requirement that the total energy of such a solution must increase under small variations in the scale factor  $a$ )

$$\left. \frac{d^2(\rho a^3)}{da^2} \right|_{a=1} > 0 \quad (\text{D19})$$

is always satisfied for  $\vec{B} \neq 0$ , since  $\mathbb{H}$  has no negative eigenvalues. As energy minima, such solutions must also satisfy

$$\left. \frac{d(\rho a^3)}{da} \right|_{a=1} = 0 \quad (\text{D20})$$

which translates to the virial theorem

$$\begin{aligned}\langle G_{ab} \nabla \theta^a \cdot \nabla \theta^b \rangle \\ = \langle \vec{B}^2 + H_{ab} (\vec{A} \times \nabla \theta^a) \cdot (\vec{A} \times \nabla \theta^b) \rangle\end{aligned}\quad (\text{D21})$$

When  $\vec{A} = 0$ , this implies  $\nabla \theta^a = 0$ , i.e. we get back Derrick's theorem. In the general case,  $\vec{\theta}$  gradients would become dominating as the scale factor  $a$  grows, since their energy density scales as  $1/a^2$ , while the energy density of the terms on the right hand side scales as  $1/a^4$ .

## APPENDIX E: PHOTON DEFLECTION

Besides causing photons to decay, a variable  $\langle\Phi\rangle$  background can deflect their trajectories. For small gradients, we can use perturbation theory to study how they scatter radiation. To first order, the scattered field  $\vec{A}^1$  created by a perturbation  $\hat{\mathbb{F}}$  of the differential operator  $\hat{\mathbb{D}}$  acting on  $\vec{A}^0$  is

$$\vec{A}^1(x) = \int d^4y \mathbb{G}(x, y) \hat{\mathbb{F}}(y) \vec{A}^0(y) \quad (\text{E1})$$

where  $\mathbb{G}$  is the Green's function associated with  $\hat{\mathbb{D}}$ . To compute it, we read off  $\hat{\mathbb{D}}$  from the Euler-Lagrange equations for  $\vec{A}$  in the time-axial gauge,

$$\hat{D}_{mn} A_n = \hat{F}_{mn} A_n \quad (\text{E2})$$

where

$$\hat{D}_{mn} = \delta_{mn} (\partial_0^2 - \partial_j \partial_j) + \partial_m \partial_n \quad (\text{E3})$$

and (using Cartesian field coordinates for the scalars, Eq. (C1); see also [54])

$$\begin{aligned} \hat{F}_{mn} &= \frac{\dot{a}}{a} \delta_{mn} \partial_0 \\ &+ \mathcal{H}^{kl} \delta_{mn} (\dot{\phi}^k \dot{\phi}^l - \partial_j \phi^k \partial_j \phi^l) \\ &+ \mathcal{H}^{kl} \partial_m \phi^k \partial_n \phi^l \end{aligned} \quad (\text{E4})$$

where indices now run from 0 to 3 and  $\mathcal{H}^{kl}$  are the components of the  $4 \times 4$  matrix analogous to  $\mathbb{H}$ . By choice,  $\hat{\mathbb{D}}$  contains only spacetime-independent terms. The Green's function can therefore be written as the Fourier integral

$$G_{mn}(\vec{x}, t) = \int \frac{d^3p}{(2\pi)^3} \frac{d\omega}{2\pi} e^{i(\vec{p} \cdot \vec{x} - \omega t)} \mathcal{G}_{mn}(\vec{p}, \omega) \quad (\text{E5})$$

satisfying

$$\hat{D}_{km} G_{mn}(\vec{x}, t) = \delta_{kn} \delta(\vec{x}, t) \quad (\text{E6})$$

which implies

$$[\delta_{km}(\omega^2 - \vec{p}^2) + p_k p_m] \mathcal{G}_{mn}(\vec{p}, \omega) = -\delta_{kn} \quad (\text{E7})$$

and therefore

$$\mathcal{G}_{mn}(\vec{p}, \omega) = \frac{p_m p_n - \omega^2 \delta_{mn}}{\omega^2(\omega^2 - \vec{p}^2)} \quad (\text{E8})$$

(strictly speaking, this needs to be augmented with a prescription for handling the poles at  $\omega^2 = 0$  and at  $\omega^2 = \vec{p}^2$ , but doing so turns out to be unnecessary for the task at hand). Changing order of integration, the scattered field can now be written as

$$\begin{aligned} \vec{A}^1(\vec{x}, t) &= \int \frac{d^3p}{(2\pi)^3} \frac{d\omega}{2\pi} e^{i(\vec{p} \cdot \vec{x} - \omega t)} \mathcal{G}(\vec{p}, \omega) \\ &\int d^3y d\tau e^{-i(\vec{p} \cdot \vec{y} - \omega \tau)} \hat{\mathbb{F}}(\vec{y}, \tau) \vec{A}^0(\vec{y}, \tau) \end{aligned} \quad (\text{E9})$$

The last integral is just the Fourier transform of  $\hat{\mathbb{F}} \vec{A}^0$ , which has elements

$$\begin{aligned} \hat{\mathbb{F}}_{mn} A_n^0 &= \left\{ -i\Omega \frac{\dot{a}}{a} \delta_{mn} \right. \\ &\quad + \mathcal{H}^{kl} (\dot{\phi}^k \dot{\phi}^l - \partial_j \phi^k \partial_j \phi^l) \delta_{mn} \\ &\quad \left. + \mathcal{H}^{kl} \partial_m \phi^k \partial_n \phi^l \right\} A_n^0 \end{aligned} \quad (\text{E10})$$

Having effectively reduced the operator  $\hat{\mathbb{F}}$  to an ordinary matrix  $\mathbb{F}$  (with elements given by the terms inside curly brackets) multiplying  $\vec{A}^0$  we can handle the Fourier transform as an ordinary convolution

$$\begin{aligned} \int d^3y d\tau e^{-i(\vec{p} \cdot \vec{y} - \omega \tau)} \mathbb{F}(\vec{y}, \tau) \vec{A}^0(\vec{y}, \tau) \\ = \frac{1}{(2\pi)^4} \mathcal{F} * \vec{\mathcal{A}}_0(\vec{p}, \omega) \end{aligned} \quad (\text{E11})$$

where  $\mathcal{F}$  is the Fourier transform of the matrix  $\mathbb{F}$  and  $\vec{\mathcal{A}}^0$  is the Fourier transform of  $\vec{A}^0$ .

A convenient choice of  $\vec{A}^0$  is the infinite plane wave

$$\vec{A}^0(\vec{x}, t) = \vec{A}^0(\vec{0}, 0) e^{i(\vec{\Pi} \cdot \vec{x} - \Omega t)} \quad (\text{E12})$$

with  $\vec{\mathcal{A}}$  constant (we are entering the usual, implicit agreement familiar to electrical engineers that the real and imaginary parts represent separate solutions which can be extracted at the end of the calculation). Any well-behaved vector field can be built by summing such waves, so our conclusion will be of general validity. With this  $\vec{A}^0$ ,

$$\vec{\mathcal{A}}^0(\vec{p}, \omega) = \vec{A}^0(\vec{0}, 0) (2\pi)^4 \delta(\vec{\Pi} - \vec{p}, \Omega - \omega) \quad (\text{E13})$$

and so

$$\mathcal{F} * \vec{\mathcal{A}}^0(\vec{p}, \omega) = (2\pi)^4 \mathcal{F}(\vec{p} - \vec{\Pi}, \omega - \Omega) \vec{A}^0(\vec{0}, 0) \quad (\text{E14})$$

by which

$$\begin{aligned} \vec{A}^1(\vec{x}, t) &= \int \frac{d^3p}{(2\pi)^3} \frac{d\omega}{2\pi} e^{i(\vec{p} \cdot \vec{x} - \omega t)} \mathcal{G}(\vec{p}, \omega) \mathcal{F}(\vec{p} - \vec{\Pi}, \omega - \Omega) \\ &\quad \cdot \vec{A}^0(\vec{0}, 0) \\ &= \int \frac{d^3p}{(2\pi)^3} \frac{d\omega}{2\pi} e^{i(\vec{p} \cdot \vec{x} - \omega t)} \mathcal{G}(\vec{p} + \vec{\Pi}, \omega + \Omega) \mathcal{F}(\vec{p}, \omega) \\ &\quad \cdot \vec{A}^0(\vec{x}, t) \end{aligned} \quad (\text{E15})$$

To compare the directions of propagation of  $\vec{A}^0$  and of the total field  $\vec{A}^0 + \vec{A}^1$  we can compute their Poynting vectors

$$\vec{S} = \vec{E} \times \vec{B} = -\vec{A} \times \nabla \times \vec{A} \quad (\text{E16})$$

and the angle between them:

$$|\vec{S}^0 \times \vec{S}| = |\vec{S}^0| |\vec{S}| \sin(\theta) \quad (\text{E17})$$



In general, this is too hard to do analytically, but suppose  $\phi^k(t, x)$  and  $a(t)$  are slowly varying on the scale of  $\vec{\Pi}$  and  $\Omega$  (and above), i.e.  $\mathcal{F}(\vec{p} \geq \vec{\Pi}, \omega \geq \Omega) \simeq 0$  and the integral is dominated by contributions from the region  $p \ll \Pi$ ,  $\omega \ll \Omega$ . We can then use the ray optics approximation  $\mathcal{G}(\vec{p} + \vec{\Pi}, \omega + \Omega) \simeq \mathcal{G}(\vec{\Pi}, \Omega)$  and write

$$\begin{aligned} \vec{A}^1(\vec{x}, t) &\simeq \mathcal{G}(\vec{\Pi}, \Omega) \int \frac{d^3p}{(2\pi)^3} \frac{d\omega}{2\pi} e^{i(\vec{p} \cdot \vec{x} - \omega t)} \mathcal{F}(\vec{p}, \omega) \\ &\quad \cdot \vec{A}^0(\vec{x}, t) \\ &= \mathcal{G}(\vec{\Pi}, \Omega) \mathbb{F}(\vec{x}, t) \vec{A}^0(\vec{x}, t) \end{aligned} \quad (\text{E18})$$

With our plane wave  $\vec{A}^0(\vec{x}, t)$ ,

$$\dot{\vec{A}}^0 = -i\Omega \vec{A}^0 \quad (\text{E19})$$

$$\partial_k \vec{A}^0 = i\Pi_k \vec{A}^0 \quad (\text{E20})$$

so

$$\vec{S}^0 = \Omega \left( \vec{A}^0 \cdot \vec{\Pi} \vec{A}^0 - \vec{A}^0 \cdot \vec{A}^0 \vec{\Pi} \right) \quad (\text{E21})$$

Without loss of generality, we can align the  $z$  axis with  $\vec{\Pi}$ ,  $\vec{\Pi} = \Pi \hat{z}$ . Absent longitudinal polarization in  $\vec{A}^0$ , this implies  $\vec{A}_3^0 = 0$  and makes  $\mathcal{G}(\Pi \hat{z}, \Omega)$  diagonal. It is then straightforward to compute  $\sin(\theta)$  in the limit  $\partial_\mu \mathbb{F} = 0$  and find that it vanishes when the dispersion relation  $\Pi^2 = \Omega^2$  is imposed. The first finite contribution is  $\propto \partial_\mu \mathbb{F}$ , i.e. third order in derivatives of  $\Phi$ , and relatively messy. For real  $\vec{A}^0(\vec{0}, 0)$ , again imposing  $\Pi^2 = \Omega^2$  and keeping only leading order terms in  $\Omega$ , it reduces to

$$\begin{aligned} \sin(\theta) &\simeq \left( \left| \vec{A}^0(\vec{0}, 0) \right| \frac{\dot{a}}{a} \Omega^2 \right)^{-1} \\ &\quad \cdot \left| A_1^0(\vec{0}, 0)(\partial_2 F_{11} - \partial_1 F_{12}) \right. \\ &\quad \left. + A_2^0(\vec{0}, 0)(\partial_2 F_{12} - \partial_1 F_{22}) \right| \end{aligned} \quad (\text{E22})$$

Whether this is a good approximation depends on the relation between Hubble parameter  $\dot{a}/a$  and derivatives of  $\Phi$ . If we are to believe astronomers, the current expansion rate is  $\dot{a}/a \simeq 70 \text{ km/s/Mpc} \simeq 4.6 \cdot 10^{-26} \text{ eV}$ . The

photon mass bound quoted by the Particle Data Group (PDG) in 2010 [80] (based on the solar wind at Pluto's orbit [81]) is  $m_\gamma < 10^{-18} \text{ eV}$ . A more conservative bound obtained by looking for deviations from Coulomb's law in the laboratory is  $m_\gamma < 10^{-14} \text{ eV}$  [82]. Using the PDG limit,  $\partial_\mu \Phi \sim m_\gamma \sim 10^{-18} \text{ eV}$  yields  $\mathbb{F} \sim 10^{-36} \text{ eV}^2$ . For  $\Omega \sim 1 \text{ eV}$ , terms  $\propto \Omega \dot{a}/a$  then dominate over terms  $\propto \mathbb{F}$ .

If we nevertheless drop all terms involving the Hubble parameter, the result becomes exactly  $\propto 1/\Omega$ , with

$$\begin{aligned} \left| \vec{A}^0(\vec{0}, 0) \right| \frac{\dot{a}}{a} \Omega^2 &\rightarrow \\ \Omega \left[ \left( F_{11} A_1^0(\vec{0}, 0) + F_{12} A_2^0(\vec{0}, 0) \right)^2 \right. \\ &\quad \left. + \left( F_{12} A_1^0(\vec{0}, 0) + F_{22} A_2^0(\vec{0}, 0) \right)^2 \right]^{\frac{1}{2}} \end{aligned} \quad (\text{E23})$$

in the expression above. Note that  $\sin(\theta)$  is now  $\propto$  derivatives of  $\Phi$ . For linear polarization (e.g.  $A_2^0 = 0$ ), it reduces to

$$\sin(\theta) \simeq \frac{|\partial_2 F_{11} - \partial_1 F_{12}|}{\Omega \sqrt{F_{11}^2 + F_{12}^2}} \quad (\text{E24})$$

Even so, deflection clearly remains negligibly small for  $m_\gamma \sim \partial_\mu \Phi \sim 10^{-18} \text{ eV}$  and  $\Omega \sim 1 \text{ eV}$ . The difference between deflected and undeflected angular positions seen by an observer can never be larger than the deflection angle, so we can use the angular resolution of astronomical observations for a comparison. Earth-based telescopes resolve angles of about 0.4 arcseconds, or  $2 \cdot 10^{-6}$  radians. The Hubble space telescope's design target was a resolution of 0.1 arcseconds.

Turning this around, it would take an effective photon mass  $\sim 10^{-6} \text{ eV}$  or more to cause deflection directly detectable with current telescopes. Since that's equivalent to a wavelength of  $\sim 1 \text{ m}$  or less, it would presumably require a  $\Phi$  configuration stabilized by electromagnetic fields (or something else) in order to be long-lived. A traveling plane wave of the kind discussed by van Holten [63]–[66] might also do.

---

[1] R. Penrose (2004) *The Road to Reality*, 744–746, Knopf, New York.  
[2] D.A. Kirzhnits, A.D. Linde (1972) Phys. Lett. B42, 471.  
[3] L. Dolan, R. Jackiw (1974) Phys. Rev. D9, 3320.  
[4] S. Weinberg (1974) Phys. Rev. D9, 3357.  
[5] T.W.B. Kibble (1976) J. Phys. A9, 1387.  
[6] E.R. Harrison (1987) *Darkness at Night: A Riddle of the Universe*, Harvard University Press.  
[7] A.E. Everett (1974) Phys. Rev. D10, 3161.  
[8] J.A. Harvey, E.W. Kolb, D.B. Reiss, S. Wolfram (1982) Nucl. Phys. B201, 16.

[9] T. Vachaspati, A. Vilenkin (1984) Phys. Rev. D30, 2036.  
[10] T. Appelquist, J. Carazzone (1975) Phys. Rev. D11, 2856.  
[11] S. Weinberg (1980) Phys. Lett. B91, 51.  
[12] H. Georgi (1994) Ann. Rev. Nucl. Part. Sci. 43, 209.  
[13] D.Y. Grigoriev, V.A. Rubakov (1988) Nucl. Phys. B299, 67.  
[14] G. Felder, L. Kofman, A. Linde (2001) Phys. Rev. D64, 123517 (<http://arxiv.org/abs/hep-th/0106179>).  
[15] A. Rajantie (2002) Int. J. Mod. Phys. A17, 1 (<http://arxiv.org/abs/hep-ph/0108159>).

- [16] C. Montonen (1978) Nucl. Phys. B140, 333.
- [17] G. 't Hooft (1981) Nucl. Phys. B190, 455.
- [18] M.N. Chernodub, L.D. Faddeev, A.J. Niemi (2008) JHEP 12, 014 (<http://arxiv.org/abs/0804.1544>).
- [19] S. Weinberg (1996) *The Quantum Theory of Fields, Vol II*, Cambridge University Press.
- [20] R.F. Dashen, B. Hasslacher, A. Neveu (1974) Phys. Rev. D10, 4138.
- [21] Y. Nambu (1977) Nucl. Phys. B130, 505.
- [22] N.S. Manton (1983) Phys. Rev. D28, 2019.
- [23] F.R. Klinkhamer, N.S. Manton (1984) Phys. Rev. D30, 2212.
- [24] L. Yaffe (1989) Phys. Rev. D40, 3463.
- [25] F. Klinkhamer (1993) Nucl. Phys. B410, 343 (<http://arxiv.org/abs/hep-ph/9306295>).
- [26] F. R. Klinkhamer, P. Olesen (1994) Nucl. Phys. B422, 227 (<http://arxiv.org/abs/hep-ph/9402207>).
- [27] M. Barriola, T. Vachaspati, M. Bucher (1994) Phys. Rev. D50, 2819 (<http://arxiv.org/abs/hep-th/9306120>).
- [28] T. Vachaspati, G.B. Field (1994) Phys. Rev. Lett. 73, 373 (<http://arxiv.org/abs/hep-ph/9401220>).
- [29] N.F. Lepora, T.W.B. Kibble (1999) JHEP 9904, 027 (<http://arxiv.org/abs/hep-th/9904178>).
- [30] B. Kleihaus, J. Kunz, K. Myklevoll (2004) Phys. Lett. B582, 187 (<http://arxiv.org/abs/hep-th/0310300>).
- [31] J. Ambjørn, T. Askgaard (1991) Nucl. Phys. B353, 346.
- [32] D.V. Gal'tsov, M.S. Volkov (1991) Phys. Lett. B273, 255.
- [33] T.S. Biro, C. Gong, B. Mueller, A. Trayanov (1993) Int. J. Mod. Phys. C5, 113 (<http://arxiv.org/abs/nuc1-th/9306002>).
- [34] A. Rajantie, P.M. Saffin, E.J. Copeland (2001) Phys. Rev. D63, 123512 (<http://arxiv.org/abs/hep-ph/0012097>).
- [35] A. Tranberg, J. Smit (2003) JHEP 0311, 016 (<http://arxiv.org/abs/hep-ph/0310342>).
- [36] N. Graham (2007) Phys. Rev. Lett. 98, 101801; *ibid.* 189904(E) (<http://arxiv.org/abs/hep-th/0610267>).
- [37] A. Diaz-Gil, J. Garcia-Bellido, M.G. Perez, A. Gonzalez-Arroyo (2008) JHEP0807, 043 (<http://arxiv.org/abs/0805.4159>).
- [38] T. Anderberg (2005), arXiv:astro-ph/0511647 (<http://arxiv.org/abs/astro-ph/0511647>).
- [39] M.J.G. Veltman (1997) *Reflections on the Higgs System*, CERN Yellow Report, Geneva.
- [40] Dürr et al. (2008) Science 322 (5905), 1224.
- [41] F.J. Dyson, Phys. Rev. 85 (1952) 631.
- [42] B. van Tent, J. Smit, A. Tranberg, JCAP 0407 (2004) 003 (<http://arxiv.org/abs/hep-ph/0404128>).
- [43] F.L. Bezrukov, M.E. Shaposhnikov, Phys. Lett. B659 (2008) 703 (<http://arxiv.org/abs/0710.3755>).
- [44] A.D. Simone, M.P. Hertzberg, F. Wilczek, Phys. Lett. B678 (2009) 1 (<http://arxiv.org/abs/0812.4946>).
- [45] C. Germani, A. Kehagias, Phys. Rev. Lett. 105 (2010) 011302 (<http://arxiv.org/abs/1003.2635>).
- [46] N.E. Ligerink, N.R. Walet, R.F. Bishop, Nucl. Phys. B (Proc. Suppl.) 63A-C (1998) 667.
- [47] A.J. Bray, Adv. Phys. 43 (1994) 357 (<http://arxiv.org/abs/cond-mat/9501089>).
- [48] S. Yu. Khlebnikov, I. I. Tkachev, Phys. Rev. Lett. 77 (1996) 219 (<http://arxiv.org/abs/hep-ph/9603378>).
- [49] A.V. Frolov, JCAP 11 (2008) 009 (<http://arxiv.org/abs/0809.4904>).
- [50] J. Sainio, Comp. Phys. Comm. 181 (2010) 906 (<http://arxiv.org/abs/0911.5692>).
- [51] J. Sainio, arXiv:1201.5029 (<http://arxiv.org/abs/1201.5029>).
- [52] E. Hairer, C. Lubich, G. Wanner, Acta Numerica (2003) 399.
- [53] T. Anderberg (2012) in preparation.
- [54] T. Anderberg (2012) in preparation.
- [55] <http://simplicial.net/hanlon/>.
- [56] J.R. Morris, Phys. Rev. D59 (1999) 023513 (<http://arxiv.org/abs/hep-ph/9810420>).
- [57] K.N. Anagnostopoulos, M. Axenides, E. G. Floratos, N. Tetradis, Phys. Rev. D64 (2001) 125006 (<http://arxiv.org/abs/hep-ph/0109080>).
- [58] R. Brandenberger, I. Halperin, A. Zhitnitsky (1998) arXiv:hep-ph/9808471 (<http://arxiv.org/abs/hep-ph/9808471>).
- [59] A.L. Macpherson, B.A. Campbell, Phys. Lett. B347 (1995) 205 (<http://arxiv.org/abs/hep-ph/9408387>).
- [60] J.A. Pearson (2010) in *Proceedings of the 45th Rencontres de Moriond* (<http://arxiv.org/abs/1010.3195>).
- [61] R. Poltis, D. Stojkovic, Phys. Rev. Lett. 105 (2010) 161301 (<http://arxiv.org/abs/1004.2704>).
- [62] I. Antoniou, L. Perivolaropoulos, JCAP 12 (2010) 012 (<http://arxiv.org/abs/1007.4347>).
- [63] J.W. van Holten, Phys. Lett. B352 (1995) 220 (<http://arxiv.org/abs/hep-th/9503085>).
- [64] J.W. van Holten, Fortsch. Phys. 45 (1997) 439 (<http://arxiv.org/abs/gr-qc/9704043>).
- [65] J.W. van Holten, Lect. Notes Phys. 541 (2000) 365 (<http://arxiv.org/abs/gr-qc/9906026>).
- [66] J.W. van Holten (2008) NIKHEF/2008-009 (<http://arxiv.org/abs/0808.0997>).
- [67] T. Anderberg (2012) in preparation.
- [68] S.L. Glashow (1961) Nucl. Phys. 22, 579.
- [69] S. Weinberg (1967) Phys. Rev. Lett. 19, 1264.
- [70] A. Salam (1968) in *Elementary Particle Physics* (Nobel Symp No. 8), ed. N. Svartholm (Almqvist and Wiksell, Stockholm).
- [71] V.K. Rohatgi (1976) *An Introduction to Probability Theory and Mathematical Statistics* (Wiley, New York).
- [72] T. Anderberg (2007), arXiv:0711.3187 (<http://arxiv.org/abs/0711.3187>).
- [73] T. Appelquist, C. Bernard (1980) Phys. Rev. D22, 200.
- [74] A. Longhitano (1980) Phys. Rev. D22, 1166.
- [75] A. Longhitano (1981) Nucl. Phys. B188, 118.
- [76] W. Kilian (2003) *Electroweak symmetry breaking: the bottom-up approach*, Springer, New York.
- [77] C. Manuel (1998) Phys. Rev. D58, 016001 (<http://arxiv.org/abs/hep-ph/9801364>).
- [78] A.M. Polyakov, JETP Lett. 12 (1970) 381.
- [79] G.H. Derrick (1952) J. Math. Phys. 5, 1252.
- [80] K. Nakamura et al. (Particle Data Group) (2010) J. Phys. G 37, 075021 (<http://pdg.lbl.gov/>).
- [81] D.D. Ryutov (2007) Plasma Phys. Control. Fusion 49, B429.
- [82] E.R. Williams, J.E. Faller, H.A. Hill (1971) Phys. Rev. Lett. 26, 721.